SCANNING TUNNELING MICROSCOPY AND SPECTROSCOPY OF WET CHEMICAL SYNTHESIZED POROUS GRAPHENE NANORIBBONS IN ULTRA-HIGH VACUUM

BY

KAITYLYN ANN PARSONS

THESIS

Submitted in partial fulfillment of the requirements
for the degree of Master of Science in Electrical and Computer Engineering
in the Graduate College of the
University of Illinois at Urbana-Champaign, 2018

Urbana, Illinois

Adviser:

Professor Joseph W. Lyding

ABSTRACT

This thesis investigates wet chemically synthesized graphene nanoribbons (GNRs) on semiconductor substrates using scanning tunneling microscopy and documents the extensive maintenance required for the ultra-high vacuum chamber systems. After venting the ultra-high vacuum chamber system to atmosphere, numerous innovations and repairs were made to the chamber. An extended titanium sublimation pump was added to the scanning tunneling microscope chamber. The preparation chamber dipstick was redesigned. Challenges arose that included taking apart the preparation chamber ion pump, replacing two turbo pumps and resolving a challenging leak. The final bake-out procedure resulted in chamber base pressure of 9×10^{-11} Torr.

Atomically precise porous GNRs are a new chemically synthesized variation for which the fabrication procedure yielding multiple pores in a single ribbon and the electronic details of the ribbon have not been reported. In this work, porous GNRs are dry contact transferred in ultrahigh vacuum to clean silicon and III-V semiconducting substrates and examined using UHV scanning tunneling microscopy (STM) and spectroscopy (STS). STM imaging confirms the expected porous structure and indicates a unique electronic feature at the graphene nanopores.

To my family, for their love and support

ACKNOWLEDGMENTS

I would like to thank Professor Joseph W. Lyding with my deepest gratitude for the opportunity to conduct research in his group. Professor Lyding has provided immeasurable support during my transition into the Department of Electrical and Computer Engineering and PhD candidacy. He has mentored me throughout the trials and tribulations of ultra-high vacuum maintenance and continues to provide deeply valued guidance in my research. I look forward to continuing to work with Professor Lyding throughout my PhD research.

I am very grateful to Dr. Adrian Radocea for passing his knowledge of STM and graphene nanoribbons on to me. I would like to thank Ximeng Liu for her discussions about graphene nanoribbons and graduate school in electrical engineering. I would also like to thank Dr. Pam Pena-Martin. She provided invaluable emotional support with her continuous cheerfulness, optimism, understanding and kindness. I am very fortunate to have met a wonderful role model so early in my graduate career. I would also like to thank members of the Lyding group for welcoming me as a group member.

Finally, I would like to thank my family and friends for all of their support. My parents have supported me with their immense love, kindness, patience and support throughout my education and especially during my graduate work. I am deeply grateful for and in awe of all that my parents do and the depth of their love. My sister continues to provide joy and laughter throughout my life. I am very fortunate to have such a loving sister who reminds me to stay calm and remain joyful.

TABLE OF CONTENTS

CHAPTER 1: INTRODUCTION

1.1 Moore's Law and Graphene

Moore's law is the observation that the transistor density in a chip will double approximately every two years [1]. Scaling below the 10nm node limit for silicon transistors introduces excessive heating and quantum effects, such as tunneling of electrons that degrade the performance of the logic device [2]. New materials are required in order to continue scaling and increasing microprocessor chip performance. Two-dimensional materials possess an inherent advantage for continued scaling and have promising electrical properties.

Two-dimensional atomic crystals were first experimentally isolated from bulk material in 2004 by K. S. Novoselov, A. K. Geim, et al. [3]. In this work, mechanical exfoliation using adhesive tape was used to pull apart layers of highly oriented pyrolytic graphite. This highly reliable procedure results in a two-dimensional monolayer of carbon atoms in a hexagonal lattice, a material known as graphene. Prior to this work, free-standing two-dimensional films were thought to be thermodynamically unstable below a critical thickness consisting of a few atomic layers [4, 5]. Typically, thin films segregate or decompose due to the decreasing film thickness and decreasing melting temperatures [6, 7]. Despite this fact, Novoselov et al. prepared a variety of two-dimensional films using micromechanical cleavage under ambient conditions following the success of graphene [8]. Van der Waals forces hold the layers together in the three-dimensional form. Repeated micromechanical cleavage breaks these weak bonds to create two-dimensional films.

The properties of graphene measured experimentally demonstrate the superiority of this material to any other two-dimensional film. Electron mobility measured at room-temperature is 2×10^5 cm^2/Vs at electron density of 2×10^{11} cm^{-2} for suspended graphene [9]. Three years later, an

electron mobility of 5×10^5 cm^2/Vs cm^2/Vs at room-temperature was achieved for encapsulated graphene which exceeds the theoretical limit of 2×10^5 cm^2/Vs [10, 11]. The intrinsic strength of graphene is 130 GPa which is very close to the theoretical value, rendering the material stronger than the strongest steel [12, 13]. Furthermore, graphene is transparent due to its low optical absorption of 2.3% and dense enough to prevent any molecule from passing through. Due to the high crystalline purity of graphene, carriers have a very long lifetime before scattering occurs [8, 14]. Graphene has a thermal conductivity greater 3,000 W/mK and can withstand electrical current densities six orders of magnitude greater than what can be withstood by copper [15]. The extremely high mobilities for both holes and electrons in graphene are highly desirable for electronic device applications; however, the lack of a bandgap due to the slight overlap between the conduction and valence bands excludes logic device applications [16].

Unlike other two-dimensional films, graphene is chemically inert and can be grown with atomic precision in the form of ribbons with widths of a few nanometers [17]. Graphene nanoribbons (GNRs) afford incredible tunability in electronic properties as a result of tailoring the ribbon geometry with atomic precision. Edge perfection minimizes scattering effects of carriers, enabling mobilities to remain very high at values of 10^3-10^5 cm^2/Vs [18]. This ultimate thin body material enables exceptional gate control. Furthermore, GNRs can have bandgaps greater than silicon, providing further motivation for exploring this novel material for logic device technology.

1.2 Graphene Nanoribbons

GNRs are atomically thin ribbons of graphene with widths on the nanometer scale. Unlike conventional semiconductors, the carrier mobilities in GNRs are symmetric with values of 10^3-10^5 cm^2/Vs [18]. These mobilities are considerably higher than the electron mobility of 1241 cm^2/Vs and the hole mobility 407 cm^2/Vs in silicon at room-temperature [19]. Quantum confinement of a sheet of graphene into a ribbon opens a bandgap that is comparable to silicon [20]. Figure 1.1 compares the hexagonal lattice of graphene and the lack of a bandgap to a thin GNR with a bandgap greater than silicon [21, 22, 23].

There are a variety of GNRs with different electronic properties. Two major types of GNRs are armchair and zigzag, characterized by the geometry of the edge. Armchair GNRs are semiconducting while zigzag GNRs have metallic edge states and a semiconducting interior [24, 25]. Chiral GNRs periodically alternate the zigzag and armchair edge terminations [26]. Aside from these edge termination differences, GNRs also exist with different backbone shapes such as straight, chevron and porous. Figure 1.2 depicts the schematic of a sheet of graphene, an armchair and a zigzag edge terminated GNR and compares a typical sheet of graphene to chiral GNRs on a gold substrate using a scanning tunneling microscope [21, 27, 22]. Furthermore, the bandgap of a GNR is tunable with the ribbon width. Figure 1.3 depicts the inverse relationship between the GNR width and bandgap E_g for lithographically patterned GNRs [20]. The inset of Figure 1.3 further demonstrates that the relative orientation of a GNR on the substrate does not affect the bandgap unlike the ribbon width.

GNR synthesis has two major approaches, top-down and bottom-up fabrication. Top-down fabrication includes chemical etching and lithographic patterning [23]. Chemical etching involves covering a sheet of graphene using a mask and etching the exposed material away [28].

Lithographic patterning uses a scanning tunneling microscope tip to cut a ribbon out of sheet of graphene [23]. Both of these processes are highly uncontrollable and result in rough edges that scatter carriers, thereby degrading carrier mobility.

Bottom-up fabrication includes chemical synthesis *ex situ* and surface-assisted synthesis *in situ*. Both bottom-up fabrication processes result in atomically precise GNRs. Surface-assisted synthesis uses a gold substrate and thermal annealing to catalytically polymerize precursor molecules, for example, into polyanthrylene chains [17]. A second thermal annealing step completes the GNR formation by means of cyclodehydrogenation.

In 2010, Cai et al. first demonstrated the fabrication of atomically precise GNRs using precursor molecules and surface-assisted coupling [17]. The molecular precursors diffuse on the substrate and combine into linear polymer chains as a result of the first thermal activation step at 200 °C. A second thermal activation step at 400 °C creates GNRs by inducing intramolecular cyclodehydrogenation. The product is straight-edge GNRs with armchair edge termination and a width denoted as N=7 which describes the number of carbon atoms that are bonded across the width. The bandgaps for these straight GNRs are predicted using DFT (DFT) as 1.6 eV for N=7, 0.7 eV for N=9 and 0.2 eV for N=11. This agrees with bandgap decreasing as the width of the nanoribbon increases. Figure 1.4 (a) portrays the schematic of the molecular precursor forming into linear polymer chains and finally GNRs via the two thermal activation steps. Figure 1.4 (b) is a scanning tunneling microscopy (STM) image of the polyanthrylene chain at T=5K and (c) is an STM image of the GNRs.

As shown in Figure 1.5, the versatility of this fabrication method is demonstrated by designing a different precursor molecule that produces chevron-type GNRs with armchair edge termination and alternating segments of N=6 and N=9. Despite the different backbone structure,

this chevron-like GNR has a bandgap of 1.6 eV. However, the zigzag shape of the ribbon results in conduction bands that are less dispersive than the straight GNRs, indicating charge carrier localization. Since the band curvature is engineered by changing the backbone structure, the effective mass of the charge carriers can be engineered.

Similarly, wet-chemical synthesis uses precursor molecules to form polyanthrylene chains and then GNRs. In 2013, Vo et al. demonstrated the fabrication of smooth armchair-edge GNRs with widths less than 1 nm in a large-scale wet-chemical synthesis *ex situ* [29]. The synthesis yield is greater than 1 g of high-aspect ratio, uniform GNRs in powder form that can then be applied to semiconducting substrates. DFT predicts these GNRs to have a bandgap of 1.6 eV. Figure 1.6 (a) illustrates the GNR structure where black are carbon atoms and white are hydrogen atoms. The unit cell is outlined with the red-dashed box. Figure 1.6 (b) provides the DFT results for the bandgap and band structure. Figure 1.6 (c) portrays the schematic formation of precursor molecules into linear polyphenylenes, followed by the formation of chevron-like, armchair edge terminated GNRs. The STM images corresponding to the polymer and the GNRs on Au (111) are included under the respective schematics. Figure 1.6 (d) shows (3) the powder form of the precursor molecule, (4) the powder form of the polyphenylenes and (5) the final powder form of the GNRs. In both processes, the precursor molecule controls the GNR width, topology and edge termination. Thus, a wide variety of GNRs are possible using bottom-up fabrication.

1.3 Scanning Tunneling Microscopy

Scanning tunneling microscopy (STM) is used for atomic resolution imaging of the topography and electronic structure of GNRs. The STM system includes an atomically sharp tip, typically tungsten or platinum-iridium, a sample holder, piezo-electronics and a feedback loop.

STMs can operate from atmospheric pressures to ultra-high vacuum [30, 31]. The temperature for a system can range anywhere from room temperature to a few kelvins above absolute zero [32, 33]. The STM system used for this thesis operates under ultra-high vacuum and at room temperature.

A bias voltage is applied between the STM tip and the substrate on which the GNRs are studied. The result is electrons tunneling through the finite potential barrier between the tip and substrate [34]. The tunneling current is dependent on the distance between the tip and sample as well as the local density of states [35]. Figure 1.7 is a schematic for the quantum tunneling effect of electrons governing the operation of the STM. Application of a negative bias with respect to the substrate results in electrons tunneling from the filled states in the substrate to empty states in the metal tip. Positive bias reverses the direction of tunneling electrons. The tip is then rastered across the substrate with atomic precision enabled by the piezo-electronics used for tip movement.

A constant tunneling current is maintained between the tip and substrate with a feedback loop and piezo-electronics. An increase in tunneling current can result from either topographically or electronically tall features. When the tip encounters either type of tall feature, the feedback loop applies an appropriate voltage to the piezo-electronics used for tip movement. A negative voltage compresses the piezo-electronic material and moves the tip away from the substrate. Once the tall feature is passed, a positive bias is applied to restore the tip's position near the substrate. Figure 1.8 is the schematic for the piezoelectric effect and the schematic for tip movement across the substrate using a feedback loop. The dotted line depicts the path of the tip. The red atoms are used to portray electronically tall features compared to the double stack of blue atoms used to illustrate topographically tall features. Figure 1.9 shows the sample holder on the STM rails brought into proximity of the STM tip.

1.4 Dry Contact Transfer

One of the major challenges for studying GNRs is a clean transfer process onto semiconductor substrates. The Lyding group developed the dry contact transfer (DCT), an unprecedented clean transfer method in which the GNRs are applied to a fiberglass DCT applicator and then stamped onto the substrate *in situ* [36]. Albrecht and Lyding first demonstrated the DCT method by depositing single-walled carbon nanotubes on hydrogen passivated silicon H:Si(100) in ultra-high vacuum for STM observations [36]. Ritter and Lyding extended the DCT method to study exfoliated graphene on silicon in which it was concluded that the edge structure of the graphene significantly affects the electronic properties of nanometer pieces of graphene [37].

This method of transfer works extremely well with the powder form of the GNRs. The GNRs are applied to the applicator *ex situ* and then loaded into ultra-high vacuum. Once in the STM chamber, the applicator is applied to the substrate surface by carefully stamping the applicator. The sample holder is then loaded onto the STM rails for the GNR experiments. Radocea et al. demonstrated the effectiveness of the DCT method for transferring chevron GNRs, provided by Sinitskii's group, *in situ* to hydrogen passivated silicon H:Si(100) [38]. The result of these experiments was high resolution characterization of the topography and electronic structure of the GNR. Figure 1.10 is a schematic with the sample holder, applicator and STM in the background.

1.5 Thesis Structure

This thesis is divided into two major projects. The first project was the complete overhaul, modification, maintenance, and bake-out to the ultra-high vacuum system used for the GNR experiments. The quality of the ultra-high vacuum and its capabilities greatly govern the success

of the experiments conducted on the GNRs. Poor quality ultra-high vacuum can introduce atmospherics and contaminants that then ruin experimental results. Once all of the modifications and repairs are complete, a process that can take a full year, the ultra-high vacuum system is then heated above 150° C for more than a week. By doing so, atmospherics and hydrocarbons will desorb from the interior surfaces of the ultra-high vacuum chambers and subsequently be pumped out.

Chapter 2 describes the detailed work on the ultra-high vacuum system. Modifications and innovations are included in the discussion. Furthermore, challenges encountered are discussed. The final result is a high quality ultra-high vacuum system. Chapter 3 presents ongoing experiments for the porous graphene nanoribbon done in collaboration with a recent graduate from the Lyding group, Dr. Radocea. Finally, chapter 4 will summarize the work presented in this thesis and provide direction for future experiments.

1.6 Figures

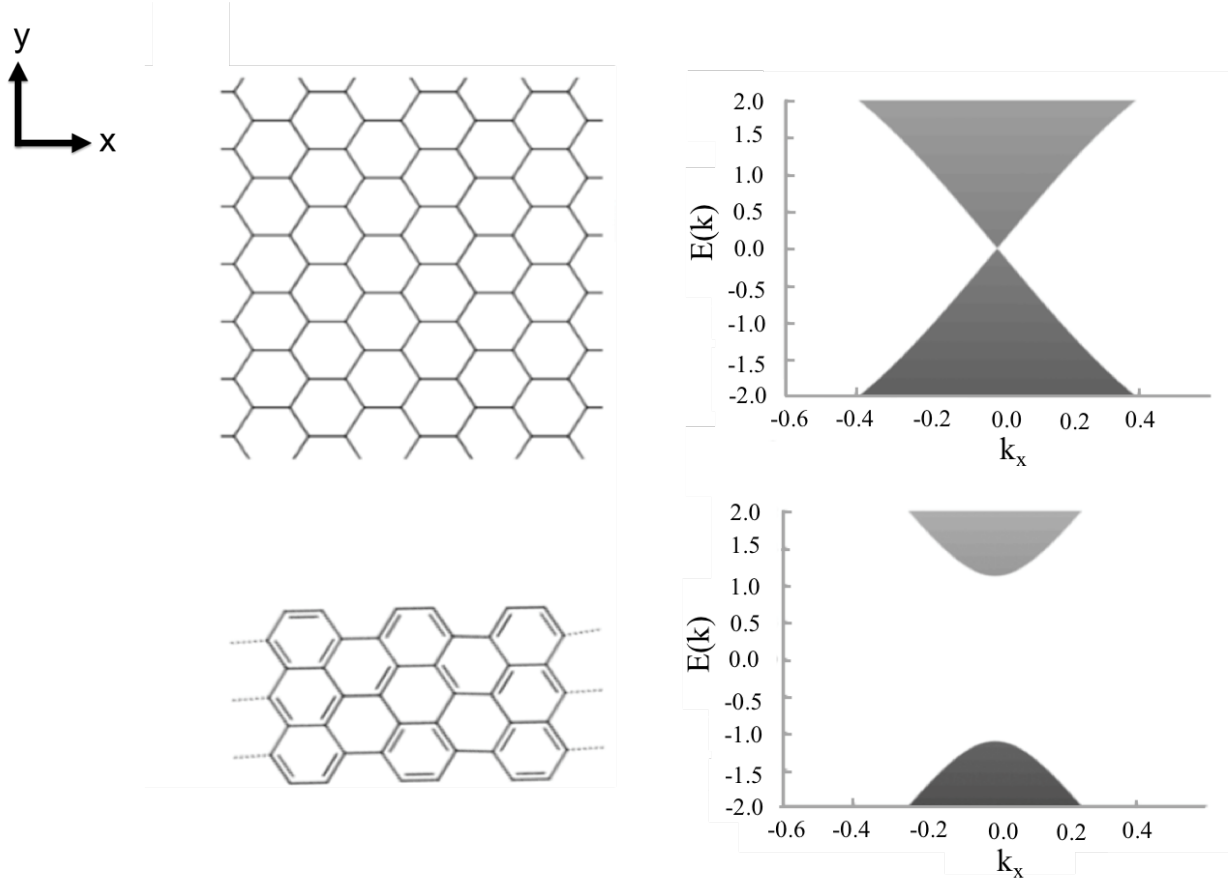

Figure 1.1 (Top) Schematic of graphene sheet and corresponding two-dimensional dispersion relation. The conduction and valence bands meet at the Dirac point rendering graphene semi-metallic and inappropriate for logic device applications. (Bottom) Schematic of N=7 GNR and corresponding two-dimensional dispersion relation. A bandgap opens as a sheet of graphene is confined to a nanoribbon with width of a few nanometers [39].

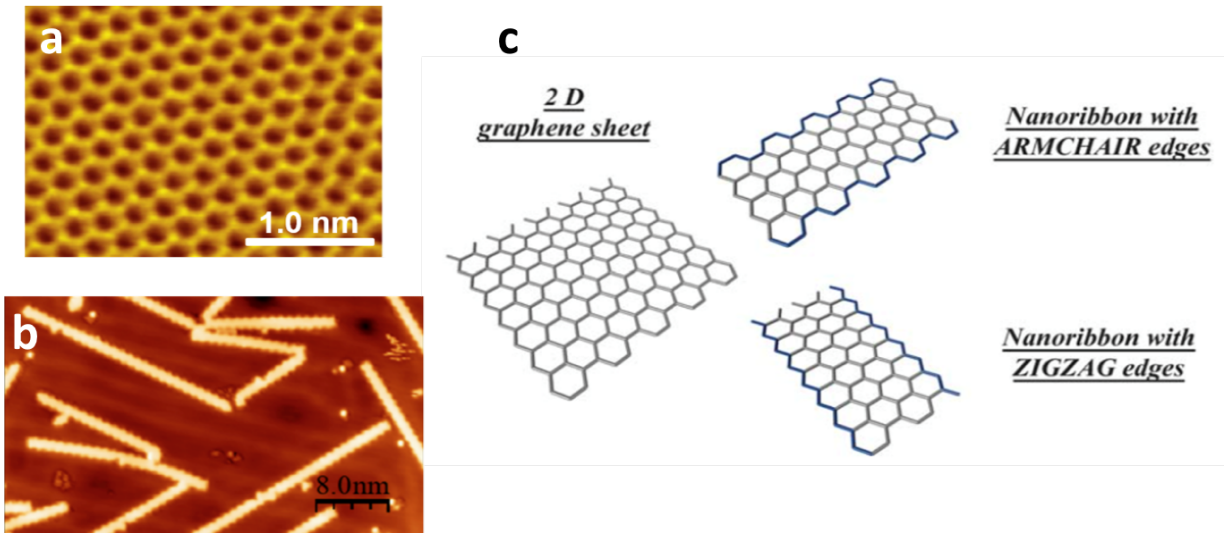

Figure 1.2 (a) STM image of a sheet of graphene. (b) STM image of chiral GNRs on a gold substrate. (c) Schematic representation of the hexagonal latticed graphene sheet, an armchair edge terminated GNR and a zigzag edge terminated GNR [21, 22, 23].

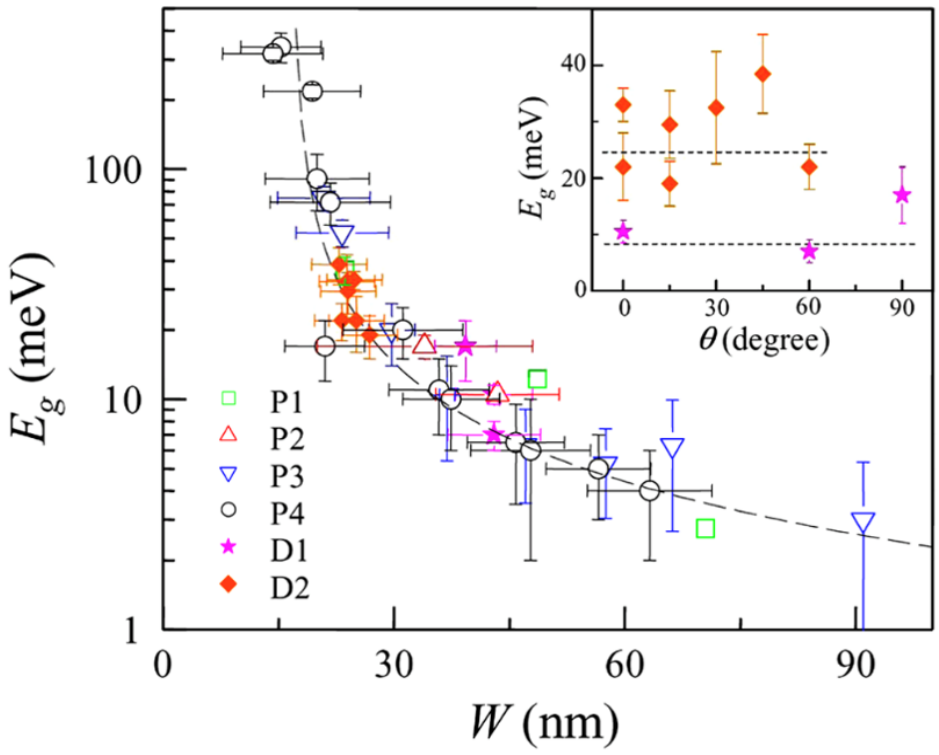

Figure 1.3 Bandgap versus width for GNRs. Decreasing the bandgap from 90 nm to 15 nm opens the bandgap by more than an order of magnitude due to quantum confinement effects. The inset demonstrates that the relative orientation on the substrate does not significantly affect the bandgap [20].

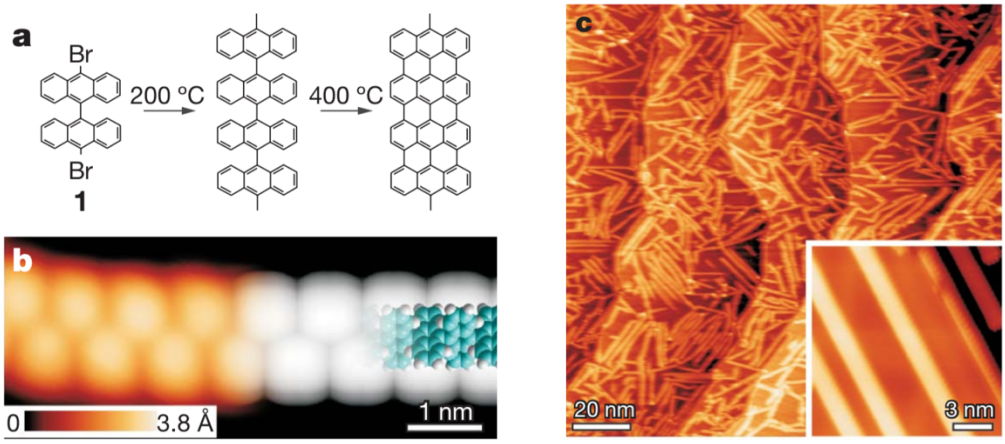

Figure 1.4 Atomically precise straight GNRs. (a) Schematic of the precursor molecule, linear polyanthrylene chain, and N=7 GNR. (b) STM image of linear polyanthrylene chain after the first annealing step (T=5 K, V=1.9 V, I=0.08 nA) with DFT simulated polymer (blue = carbon, white = hydrogen). (c) STM image of N=7 GNRs on Au(111) (T=300 K, V=-3 V, I=0.5 nA) [17].

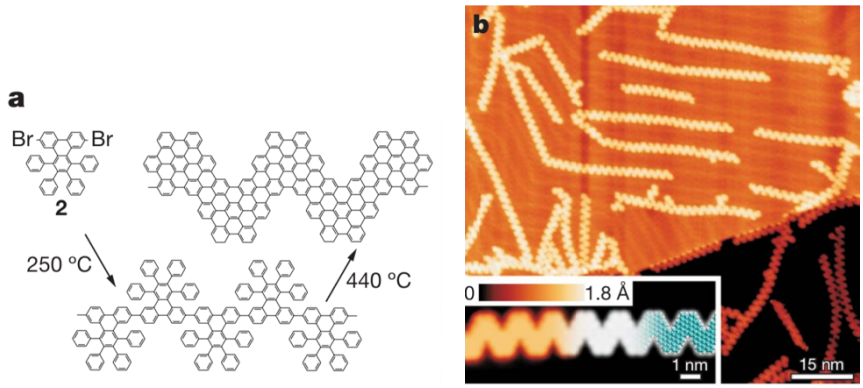

Figure 1.5 Atomically precise chevron-like GNRs. (a) Schematic of precursor molecule into a polymer chain and finally into a chevron-like GNR. (b) STM image of GNRs on Au(111) (T=35 K, V=-2 V, I=0.02 nA) and DFT simulation (blue = carbon, white = hydrogen) [17].

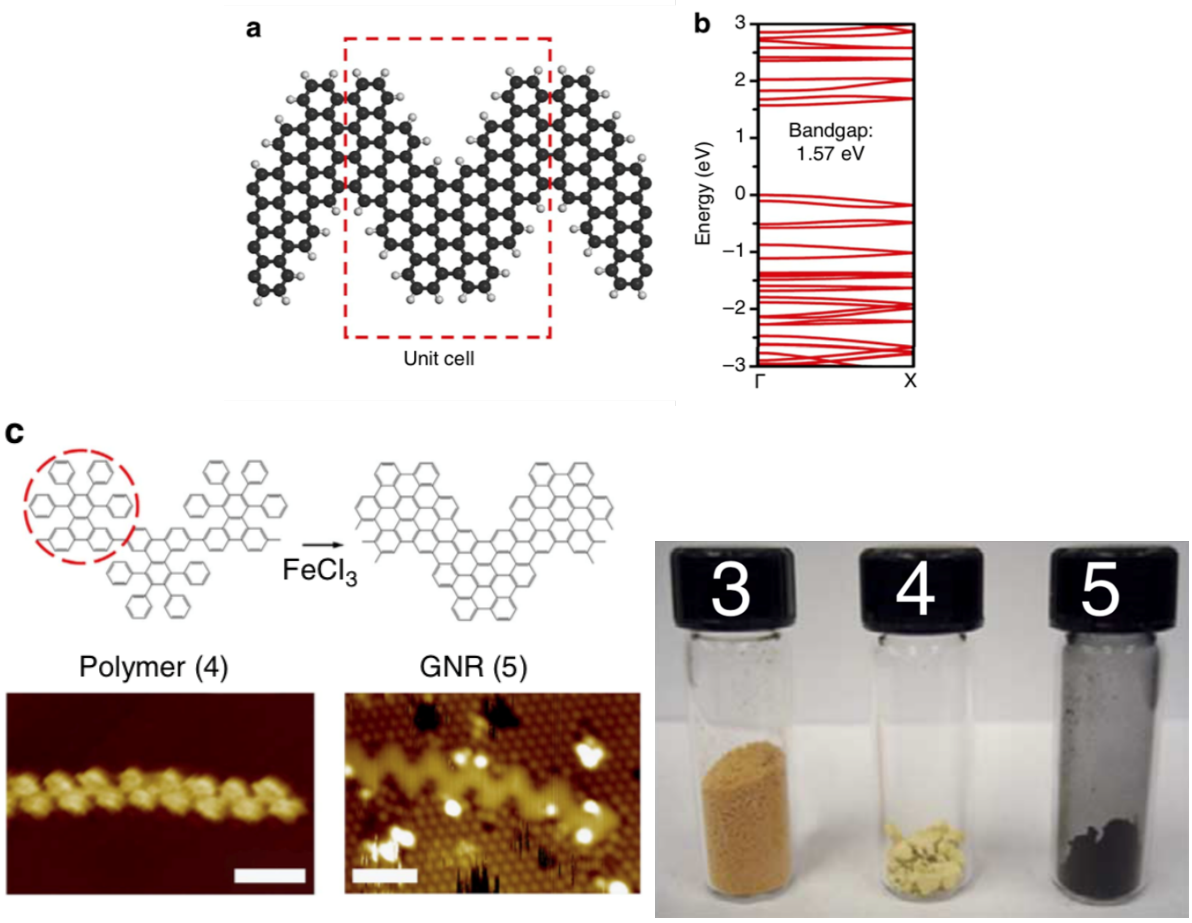

Figure 1.6 (a) Schematic of GNR with chevron backbone and armchair edge termination (black = carbon, white = hydrogen). (b) DFT simulated band structure with bandgap result of 1.57 eV. (c) Schematic of precursor molecule, polymer and GNR with STM image of the polymer (left) and STM image of the GNR on Au(111) (right). Powder form of precursor molecule (3), powder form of polymer (4), and powder form of GNR (5) [29].

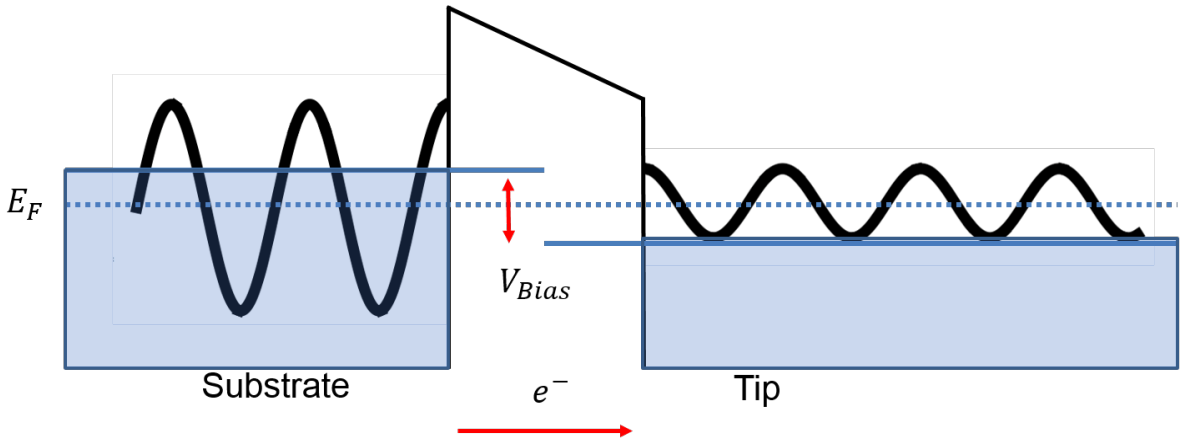

Figure 1.7 Schematic of the quantum tunneling effect governing the operation of the STM. A metal tip is brought within a few angstroms of the substrate. A bias is applied between the substrate and tip relative to the substrate resulting in the splitting of the two material's Fermi levels. For a negative bias with respect to the substrate, electrons tunnel from the filled states in the substrate to the empty states in the tip. A positive bias with respect to the substrate reverses the direction of tunneling electrons.

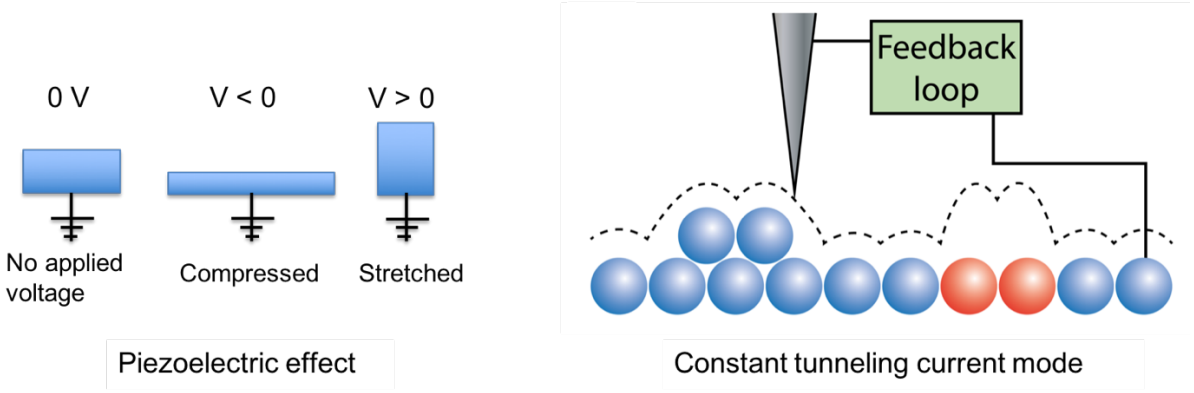

Figure 1.8 (a) Schematic of the piezoelectric effect. A negative bias compresses the piezoelectric material whereas a positive bias stretches the material. (b) Schematic of a STM tip scan across atoms. The black dashed line depicts the trail of the tip. When topographically tall features are encountered (viewed as the double layer of blue atoms), the feedback loop applies an appropriate bias to the piezoelectric material so that the tip moves away from the surface and maintains a constant tunneling current. Likewise, an electronically tall feature (viewed as the red atoms) results in higher tunneling current [40].

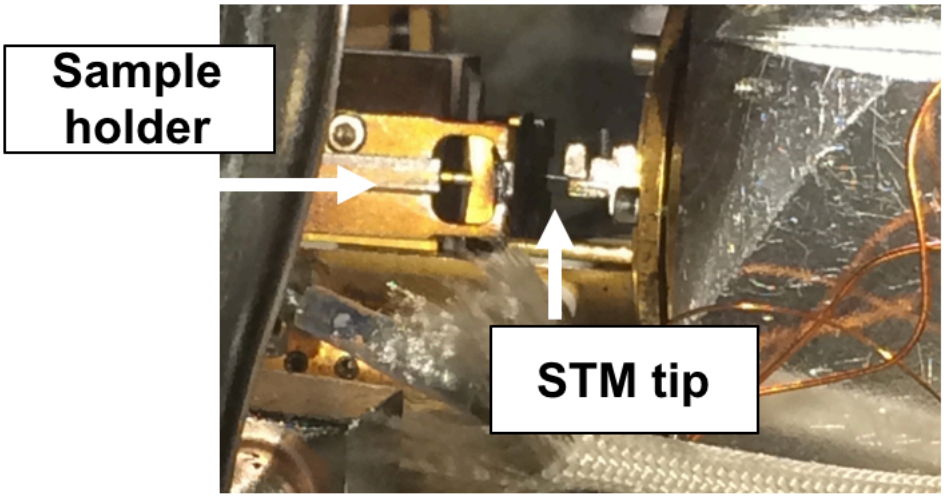

Figure 1.9 Sample holder with silicon sample on STM in ultra-high vacuum chamber system. The tip is made from tungsten and is observed in tunneling range between the silicon sample and the tip holder. The piezo-electronics are housed behind the tip holder.

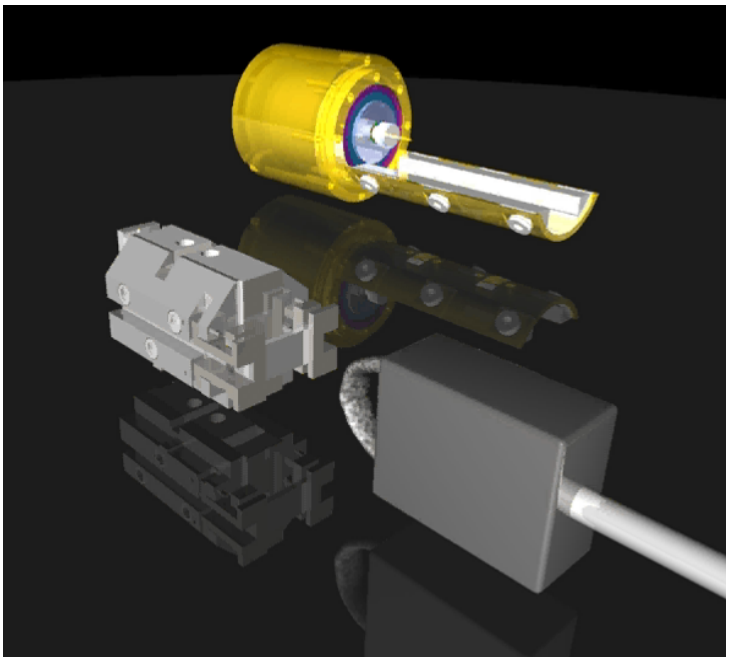

Figure 1.10 Schematic of dry contact transfer method. Sample holder is in gray on the left and fiberglass applicator is in gray on the right. The powder form of GNRs is applied to the applicator *ex situ* and then carefully stamped onto the sample holder *in situ*. The sample holder is then mounted on the STM featured in the back of the image. [Picture courtesy of Professor Lyding].

CHAPTER 2: ULTRA-HIGH VACUUM SYSTEM MAINTENANCE

2.1 Background and Motivation

Accurate experimental results rely on the quality of the ultra-high vacuum (UHV) chamber pressure. Thus, the first part of the GNRs experiments required a complete overhaul, repair and maintenance of the ultra-high vacuum system. Figure 2.1 illustrates a simplified schematic of the chamber used for the GNR experiments.

This chamber contains three main environments. The first is the load-lock which is used for transferring samples and tips from atmosphere into UHV. The gate valve between the load-lock and the preparation chamber enables isolation between ultra-high vacuum and pressures ranging between atmosphere and high-vacuum. The turbo and the roughing pump both connect to the load-lock via different lines. A nitrogen line is also connected to the load-lock. This enables venting the load-lock with an inert gas once isolation between the preparation chamber, the turbo pump and the roughing pump are achieved. By filling the load-lock with nitrogen, water cannot coat the inside and then be introduced to the ultra-high vacuum chambers.

The last two environments are the two ultra-high vacuum chambers, both of which serve different purposes. The preparation chamber is where sample and tip degassing, substrate cleaving, and substrate passivation take place. A long rod with a fork piece at the end enables linear transfer motion of samples and tips between the load-lock and into the preparation chamber. Sample and tip preparation take place on the dipstick which feeds through the top of the preparation chamber. The dipstick is isolated from atmosphere by three pumps: a roughing pump, turbo pump and then finally, the ion pump.

The STM chamber consists of a vibration isolation stage that supports the STM. Another gate valve isolates the STM chamber from the preparation chamber. A system of springs and

magnetic dampeners is used to vibrationally isolate the STM stage from the building. The STM chamber requires a robust electrical system. If an electrical short occurs as a result of time and movement on the stage, the entire ultra-high vacuum system may require an intentional atmospheric vent followed by an extensive bake-out procedure.

Both the preparation chamber and the STM chamber are connected to the turbo pump and each to its own ion pump. The connection to the turbo pump is only used for the bake-out process. Ion pumps require at least high vacuum before turning on. Once the ion pumps are running, the preparation and STM chambers are isolated from the turbo pump.

Bake-out refers to heating the entire ultra-high vacuum system to temperatures greater than 150° C. Heater tapes are wrapped around the entire system on the metal parts. If a heater tape is set across a window, the high temperatures can break the window. Sudden venting to atmosphere can then damage the ion pumps, turbo pump and pressure gauge systems. Once the heater tapes are wrapped, the entire chamber system is covered in aluminum foil to enable even heating that the low thermal conductivity of the stainless-steel system cannot achieve alone. Thermocouples are used to measure temperatures at 15 points on the system throughout the bake-out. A residual gas analyzer monitors the atmospheric gases and hydrocarbon levels. After the system has baked-out between 5-10 days, the heater tapes are turned off and the system is allowed to cool. This chapter will describe the process from first atmospheric vent to final bake-out. Figure 2.2 is the UHV chamber system during the bake-out procedure.

2.2 Modifications to the STM Chamber, Prep Chamber, and Dipstick

Extensive repairs, problem solving, and innovation were required to get this particular UHV system back on line. After venting the system to atmosphere, the top 12-inch flange was

removed and the entire STM stage and system was raised out of the chamber. The STM stage was then rebalanced by adjusting the length of various springs that suspend and vibrationally isolate the STM from the building. Rebalancing the stage is not a trivial feat. Adjusting the spring lengths affects whether the copper dampeners will short to their neighboring magnets. Furthermore, pulling the STM stage out of the chamber presents potential damage to the electrical system. Extensive electrical checks are required throughout the rebalancing procedure.

Figure 2.3 shows the STM stage suspended above the STM chamber and a zoomed-in image of the stage. The tip garage holds extra tip holders and required tightening and repair of pieces. Loose garage spots fail to securely hold the tip holders. If a tip falls out of the garage, the tip is damaged, and experiments are delayed extensively. Wire connections to the STM and above the stage are checked with meticulous care.

A major innovation added to the STM chamber was an extended titanium sublimation pump (TSP). The operational method of a titanium sublimation pump is as follows. A filament of titanium is connected to an electrical feedthrough between atmosphere and UHV. Current (I = 40 A) is passed through the titanium filament in UHV until it glows white hot. Titanium sublimes from the filament and coats the interior walls of the ultra-high vacuum chamber. When gas molecules diffusing in the ultra-high vacuum chamber collide with the interior walls, the titanium serves as a “getter atom” meaning that the diffusing gas reacts with the titanium to form inert molecules on the walls of the chamber. A liquid nitrogen shroud is often used to enhance the effectiveness of the TSP. When the shroud between the interior and exterior walls of the chamber is filled with liquid nitrogen, the diffusing gas molecules in the chamber condense to the walls and react with the titanium efficiently.

Typically, the TSP works by coating the interior walls of the chamber. Here, an extended (TSP) was designed and assembled in order to extend far enough through the pump feedthrough to evaporate titanium directly onto the bottom of the STM stage. Figure 2.4 shows the extended TSP after the design phase. A normal TSP electrical feedthrough consists of four filaments in the bottom half of the extended TSP. The use of four filaments ensures that if one filament burns out due to extensive use, there are 3 more as backups. The chamber then does not have to be vented and baked-out as frequently. The extended TSP has three filaments in the bottom half portion to coat the interior walls and an extended filament above one of the three other filaments. A copper tube is used to complete the circuit for the extended filament.

The extended TSP filament was tested in the preparation chamber at high-vacuum before the final bake-out. Figure 2.4 shows the filament glowing white hot. The bottom left image in Figure 2.4 is the top-down view of the extended TSP in the STM chamber. Once the titanium sublimes and coats the STM stage, titanium on the STM stage reacts with any impurities and keeps the base vacuum pressure low and the substrates as clean as possible.

Modifications to the preparation chamber included the implementation of a cracking filament and extensive design and repairs to the dipstick. The cracking filament is used for breaking the bonds in hydrogen molecules to produce the atomic hydrogen necessary for silicon surface passivation. Two filaments of tungsten wire were attached to copper rods on an electrical feedthrough. Figure 2.5 shows the cracking filaments. In ultra-high vacuum, current (I = 1-2 A) is passed through one of the filaments. The second filament serves as a backup in the event that the first filament burns out due to extensive use. A prepared sample, such as silicon, is in the preparation chamber during the passivation process. Hydrogen is then added to the preparation chamber through a leak valve connected to the hydrogen line and preparation chamber. The white-

hot (1500 °C) filaments react with the hydrogen molecules to create single hydrogen atoms. These atoms then react with the dangling bonds on the clean silicon surface to create hydrogen passivated silicon. Passivated silicon is required for nanolithography and GNR experiments.

The dipstick is fed through the top and into the preparation chamber and is used for degassing STM tips and substrates. A new mechanism for degassing substrates on the dipstick was designed and implemented as part of this thesis. A filament made from tantalum foil incorporated onto the dipstick indirectly degasses the substrates, mitigating damage that can occur when current is sent directly through the substrate. Inclusion of this filament was a nontrivial task due to the extensive care to not create an electrical short. Electrical connections were then added in order to directly send current through a tip carrier, thereby degassing the tips in the process. Figure 2.6 shows the long electrical feedthroughs of the dipstick as well as the implementation of the tantalum filament. The image on the right in Figure 2.6 illustrates how the tip carrier snaps into the dipstick rollers. The dipstick is then fed through bellows into the preparation chamber.

Adding the dipstick to the preparation chamber requires meticulous care so that the bellows do not snag the electrical connections or the dipstick rollers and create a short or misalignment. Once the dipstick is safely added to the preparation chamber, electrical connections must be checked before closing all of the viewing windows to the preparation chamber and baking the system out. After the electrical connections were checked, the dipstick was tested for functionality. Figure 2.7 shows the tip carrier with three tip holders degassing. In this case, current (I = 10 A) is passed directly through the carrier. The image on the right of Figure 2.7 shows the tantalum filament glowing hot when current is passed through (I = 4 A). It is imperative that not too much current is passed through the tantalum filament because this will cause the filament to blow out. A

vent and bake-out would then be required to repair the system. Tips and samples degas for at least 12 hours and cool off for at least 2 hours.

2.3 Ion Pump

The ion pump under the preparation chamber exhibited bizarre behavior, which required taking the ion pump completely apart. When the ion pump was turned off the measured resistance indicated normal operation; however, when the pump was turned on, a short circuit appeared. The eight StarCells and the non-regenerative getter appeared to operate normally. Investigations inside of the pump revealed a washer from the previous bake-out to be magnetized to the top of a StarCell holder. When the electric field was turned on, the washer was partially pulled down and made contact with the nearest StarCell. This connection resulted in grounding all of the StarCells and, hence, the presence of a short circuit only when the ion pump was on. The removal of the washer resulted in normal operation of the ion pump.

Figure 2.8 shows the connection between the ion pump and the ultra-high vacuum chamber. The electrical feedthrough is on the left and pictured with the connection cable. Resistance measurements were made here. The bottom left image in Figure 2.8 shows the ion pump removed from the ultra-high vacuum system and the bottom right image is a top-down view inside of the ion pump. The non-regenerative getter is on the bottom of the image. Four StarCells are in four cell holders on the left side and the right side.

2.4 First Bake-out Attempt

The first bake-out attempt was marked by the failure of two turbo pumps as well as the failure of atmospheric gases to decrease to tolerable pressure levels. Twenty-five heater tapes were

used to wrap the metal parts of the ultra-high vacuum system. A heater tape set across a window can result in cracking of the window, exposing the ion pumps, turbo pump and ion gauge pressure filaments to atmospheric pressure and causing considerable damage. Once the heater tapes were attached and marked by their corresponding area, aluminum foil was used to wrap the entire system in order to ensure uniform heating. The low thermal conductivity of the stainless-steel chamber requires the aluminum foil to prevent hot and cool spots. Thermocouples are used to monitor the temperature throughout the various portions of the system. Temperatures must be kept greater than 150°C for at least 5 days and up to two weeks and must not reach so high that the solder joints in the STM chamber melt. A residual gas analyzer (RGA) was used to monitor the gas levels in the ultra-high vacuum system during the bake-out process.

After the first five days, the RGA indicated a nitrogen peak reaching 1×10^{-7} Torr. At this point in the bake-out, all peaks should be around 1×10^{-9} Torr at least. The bake-out was shut off and the system was allowed to cool. A helium leak test indicated a leak at the top of the dipstick. Figure 2.9 illustrates where the leak test indicated a leak. The dipstick is isolated from atmosphere by three concentric pumping layers by the roughing, turbo and ion pumps as shown in Figure 2.10. Numerous repairs and innovations were added to the dipstick with the hope of removing the nitrogen peak in the RGA helium leak test. However, these modifications did not succeed. Investigations of the entire ultra-high vacuum system took place in order to find the source of the leak. The last place available for investigation was the roughing pump connected to the dipstick. It was discovered that the interior wall of the tube connecting the roughing pump to the dipstick collapsed. Figure 2.11 shows the roughing pump disconnected from the ultra-high vacuum system and the collapsed interior wall of the roughing pump hose. Thus, the roughing pump was incapable of pumping on the dipstick and the first line of defense between atmosphere and ultra-high vacuum

for the dipstick had failed. The leak at the top of the dipstick was therefore not an indication of a true leak, but an indication of failed pumping. Once the maintenance process was complete, the bake-out concluded with atmospheric levels below 1×10^{-11} Torr and a base pressure of 9×10^{-11} Torr.

2.5 Summary and Future Work

UHV chamber systems require extensive maintenance and meticulous care. This chamber system received repair and implementation of numerous innovations. After venting the UHV system, the STM stage was pulled out of the top of the STM chamber while suspended by a crane. Numerous repairs were performed on the STM stage, including rebalancing of the stage. An extended TSP was designed and added to the STM chamber to further keep the STM stage clean of impurities, thereby increasing the quality of experiments conducted. Two cracking filaments were added to the preparation chamber and extensive modifications were made to the dipstick.

The ion pump presented an interesting challenge. Once the washer was removed from the interior of the ion pump, normal operation was achieved. The first bake-out indicated a leak at the top of the dipstick. The collapsed interior wall of the hose connecting the roughing pump and the dipstick was revealed to be the source of the false leak. Repair of this hose allowed normal operation. The final bake-out reduced atmospheric gas levels below 1×10^{-11} Torr measured by the RGA. The final cooled off ultra-high vacuum resulted in a base pressure of 9×10^{-11} Torr.

Future work includes moving the Lyding Group STM chambers to a new lab. The four ultra-high vacuum systems will be moved one at a time. Three of the chambers will be housed in the new lab space in the Micro and Nanotechnology Laboratory (MNTL) building. The fourth chamber will be moved to the clean room in the Electrical and Computer Engineering Building

(ECEB). The goal is to move two of the chambers while maintaining UHV. However, the third chamber moving into MNTL will require dismantling and a full rebuild and bake-out once in the new lab space. The fourth STM ultra-high vacuum chamber system moving into ECEB will require clean-room admittance cleaning procedures as well as a final bake-out.

2.6 Figures

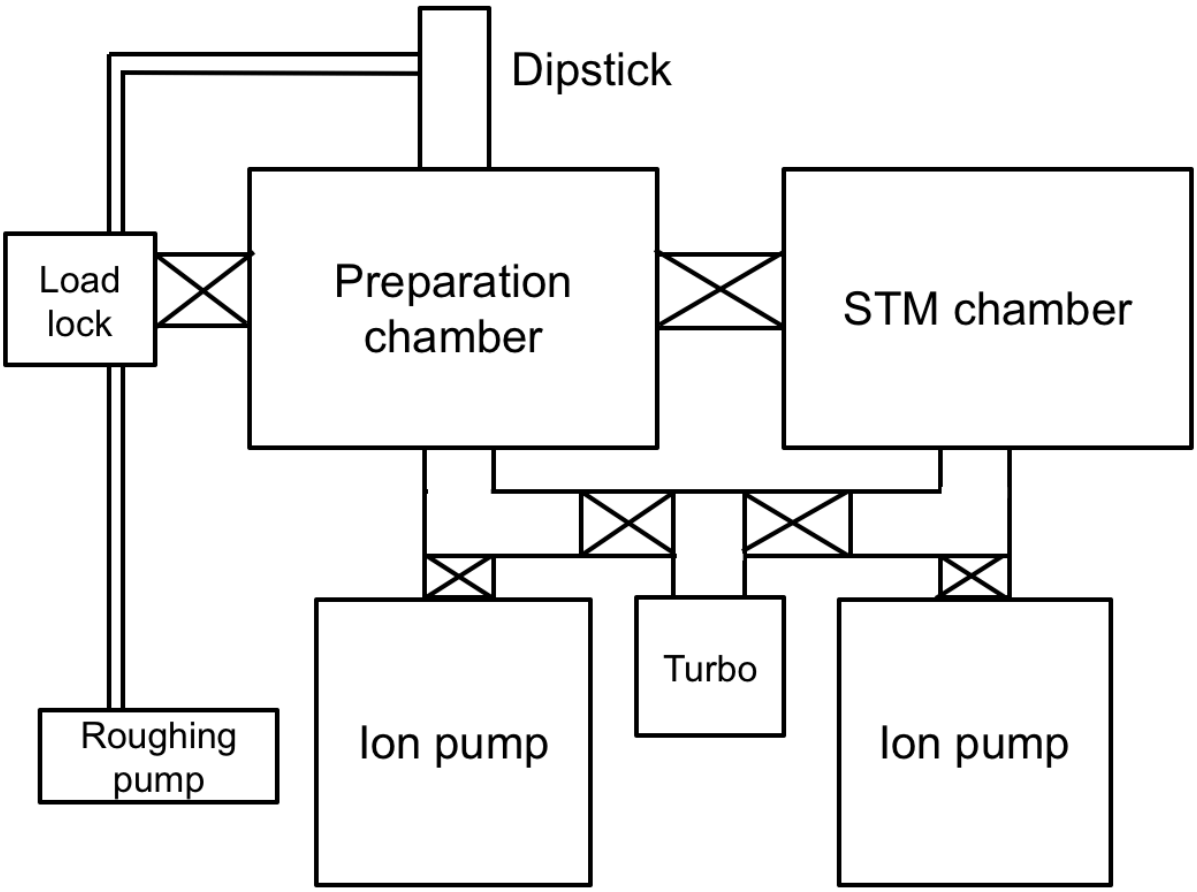

Figure 2.1 Simplified schematic of ultra-high vacuum system used for GNR experiments and to which the maintenance description corresponds. The load-lock enables transfer of tips and samples from atmosphere to ultra-high vacuum. The turbo actively pumps on the load-lock and a gate valve (black X) isolates the load-lock from the ultra-high vacuum (UHV) environment of the preparation chamber. A roughing pump line and nitrogen line are connected to the load-lock for initial pump down and venting. The preparation chamber is where tip and sample preparation take place. The dipstick is fed into the preparation chamber from atmosphere and provides electrical connections for sample and tip degassing and for surface preparation. The STM chamber is where experiments take place. Both the preparation chamber and STM chamber are actively pumped on by individual UHV ion pumps.

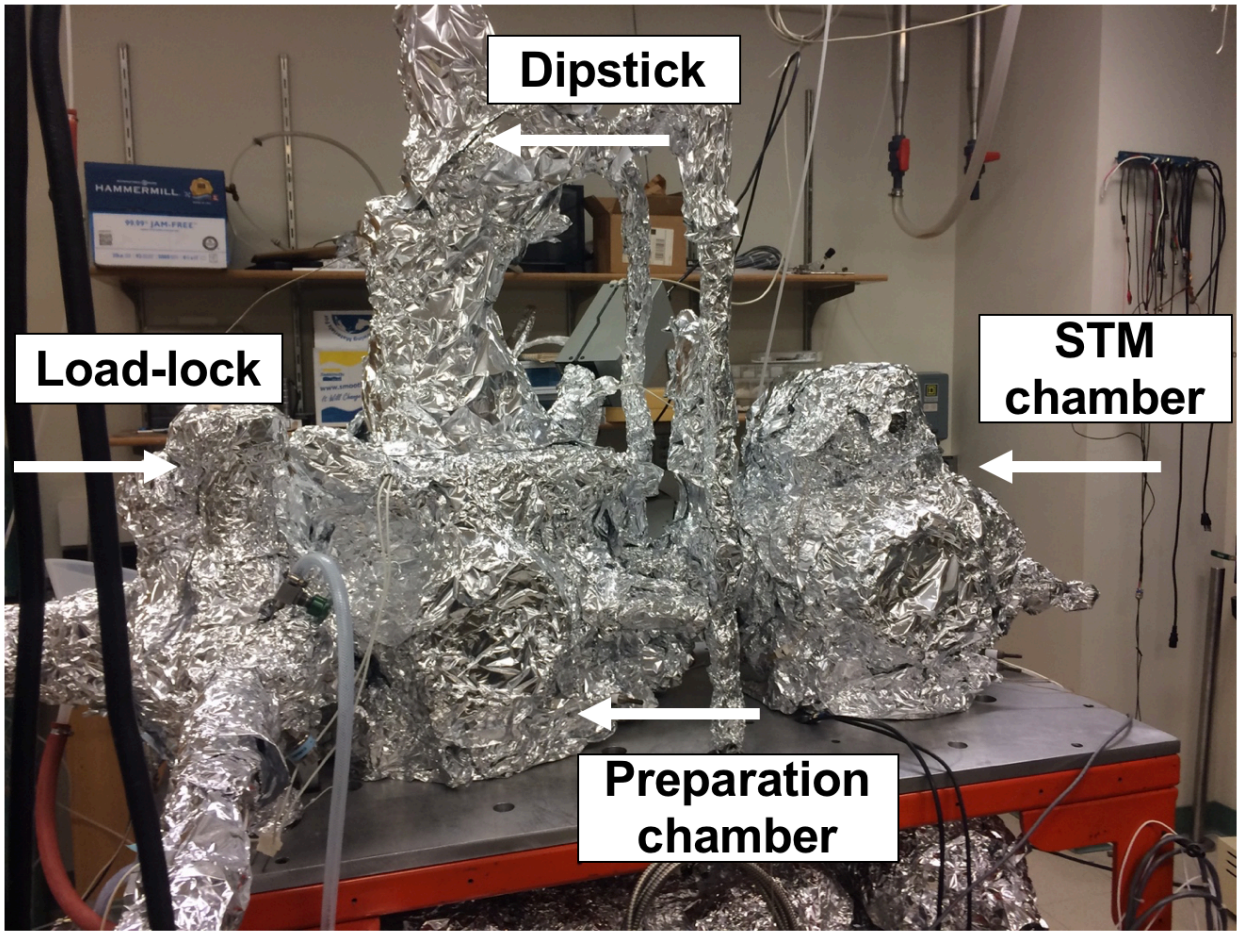

Figure 2.2 Photograph of the UHV chamber during the bake-out procedure. The low thermal conductivity of the stainless-steel chamber requires the addition of aluminum foil over the heater tapes in order to ensure even heating. The ion pumps and turbo pump are below the table and not pictured here. The roughing pump to the dipstick is on the floor behind the table and is not pictured here.

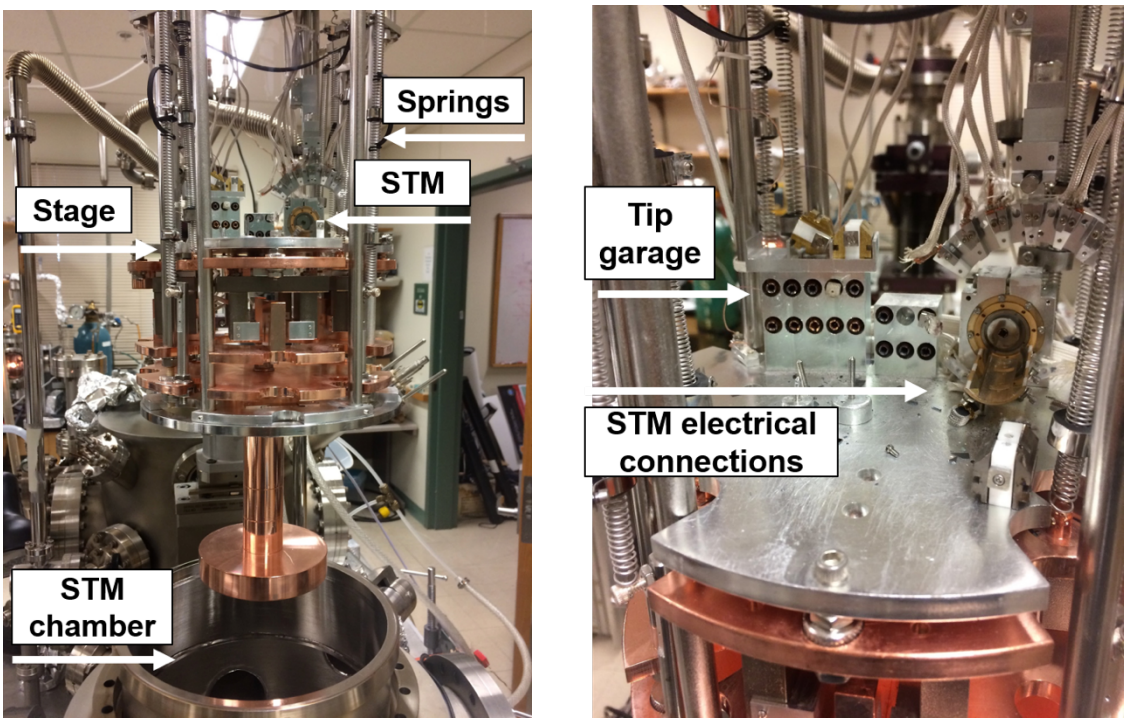

Figure 2.3 STM stage suspended above STM chamber. The STM stage was rebalanced by adjusting the spring lengths while ensuring an electrical short does not occur by the copper metal piece touching the dampening magnets below the STM stage. The zoomed-in image of the STM stage shows the tip garage, the STM and one sample holder on the stage. Repairs were made to the tip garage as well as to the STM electrical connections.

Figure 2.4 (Right) Extended TSP designed for STM stage. Titanium filaments are pictured as the silver curling rods. Three filaments are in the bottom half of the extended TSP and one filament is added to the top half. (Top left) The extended TSP is tested in the preparation chamber under high vacuum. (Bottom left) Top-down view into the STM chamber where the extended TSP is visible.

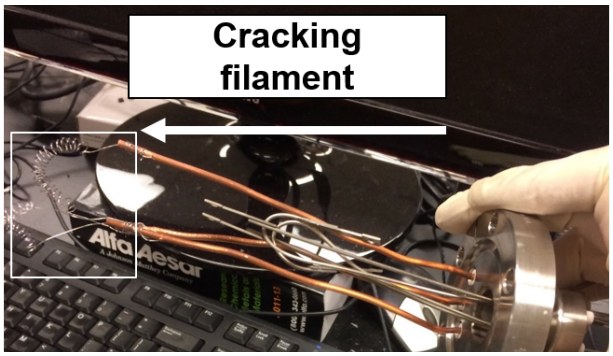

Figure 2.5 Tungsten cracking filaments used to create single hydrogen atoms from hydrogen molecules for silicon surface passivation.

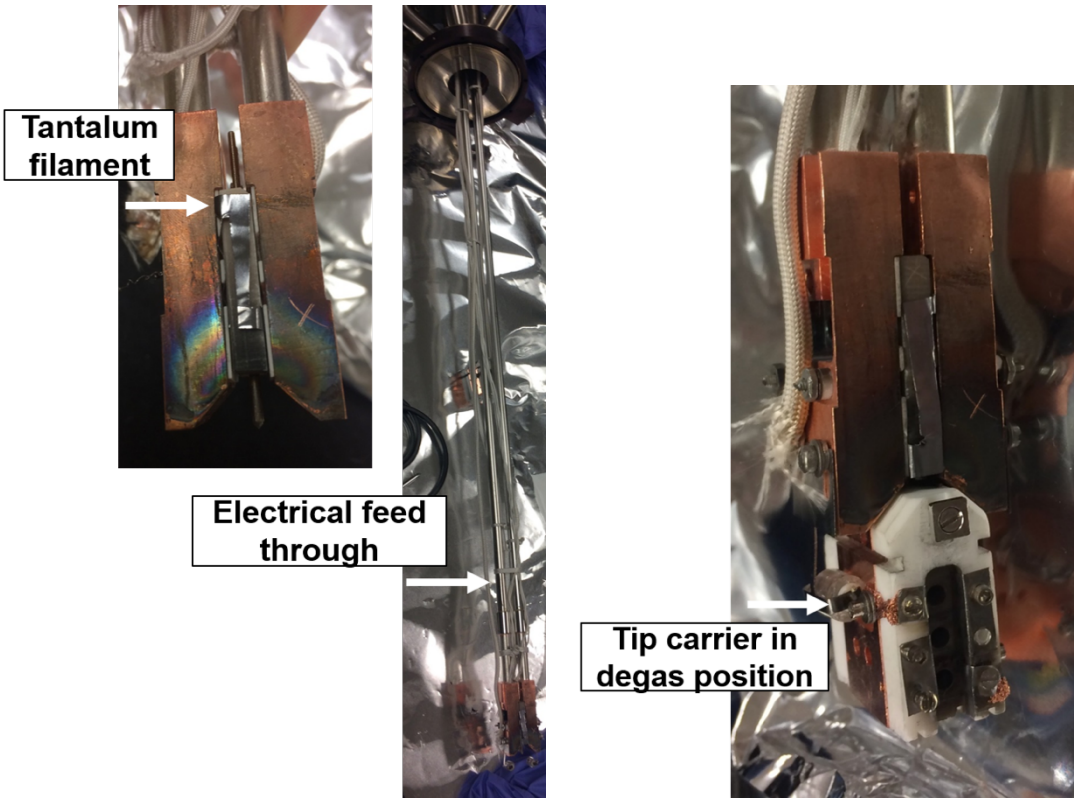

Figure 2.6 The tantalum filament used to indirectly degas samples is pictured in the far-left image. The full dipstick and length of electrical feedthroughs are observed in the middle picture. The tip carrier (right image) is held into place by the dipstick rollers. This is the degas position in which electrical feedthroughs send current directly into the tip carrier.

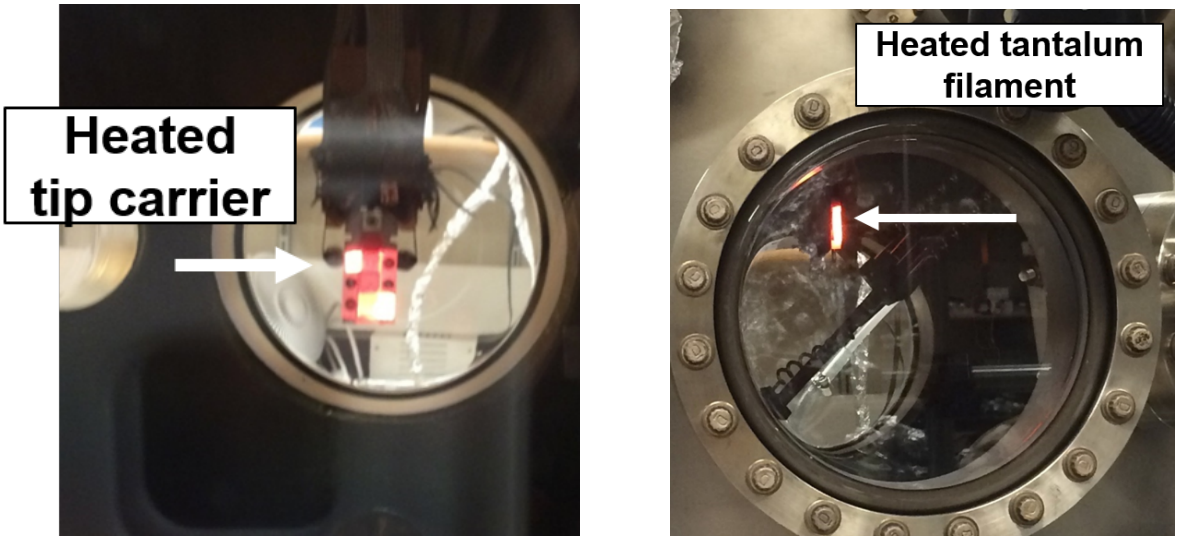

Figure 2.7 Dipstick viewed from preparation chamber viewing window. Current (I=10 A) is passed directly through the tip carrier and three tips during the degas procedure. The tantalum filament is tested in the figure on the right (I=4 A). The tantalum filament can blow out if too much current is passed through it.

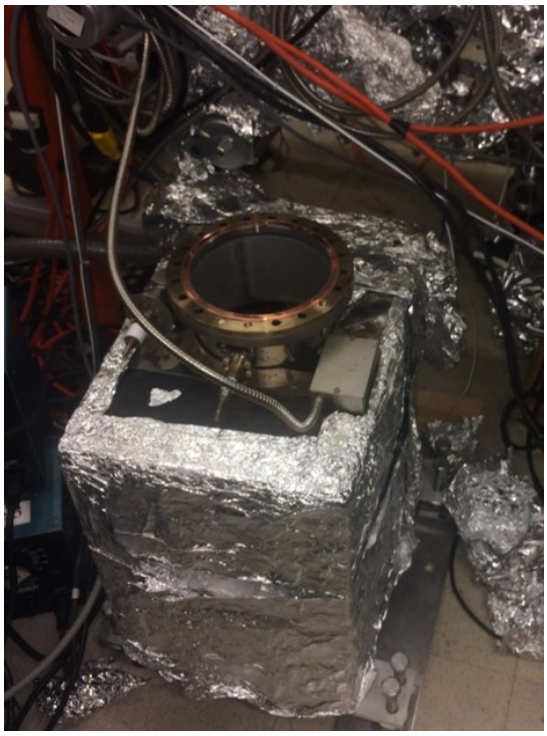

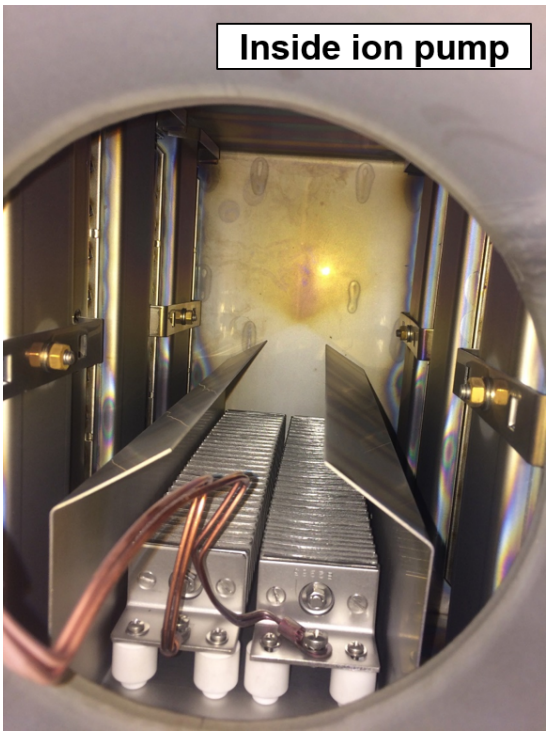

Figure 2.8 Investigation of the ion pump. (Top) Connection of ion pump to preparation chamber. The cable on the left provides the current. (Bottom left) Ion pump removed from preparation chamber. (Bottom right) Top-down view inside of the ion pump. The non-regenerative getter is at the bottom of this image. Four StarCells are in four cell holders on both the left and right sides.

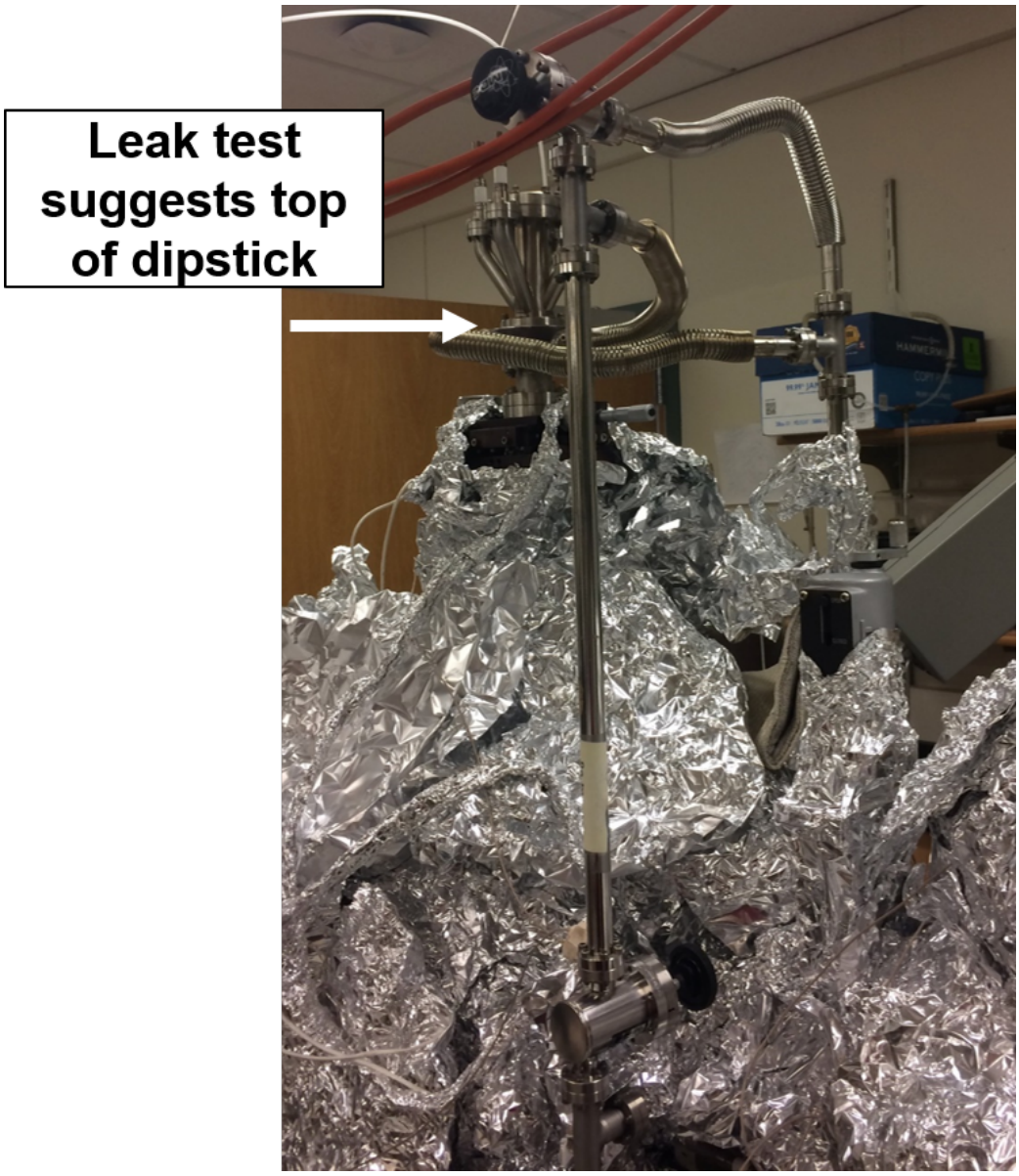

Figure 2.9 Helium leak test indicates a leak at the top of the dipstick. Numerous repairs were conducted in order to resolve the apparent leak without success.

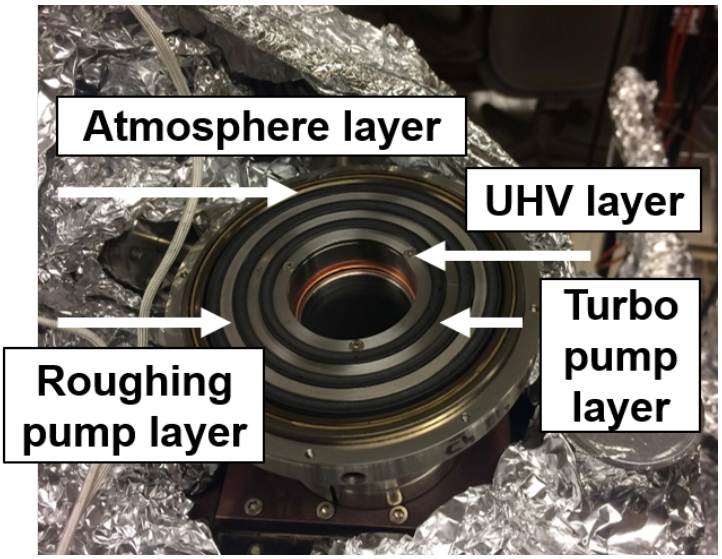

Figure 2.10 Connection between the dipstick and the preparation chamber. Three layers are used to isolate the dipstick from atmosphere to ultra-high vacuum. The outer layer is labeled as the atmosphere layer. The first line of defense is the roughing pump layer. This is followed by the turbo pump layer and finally the ultra-high vacuum (UHV) layer. The black circles are the gaskets in between the different pressure layers.

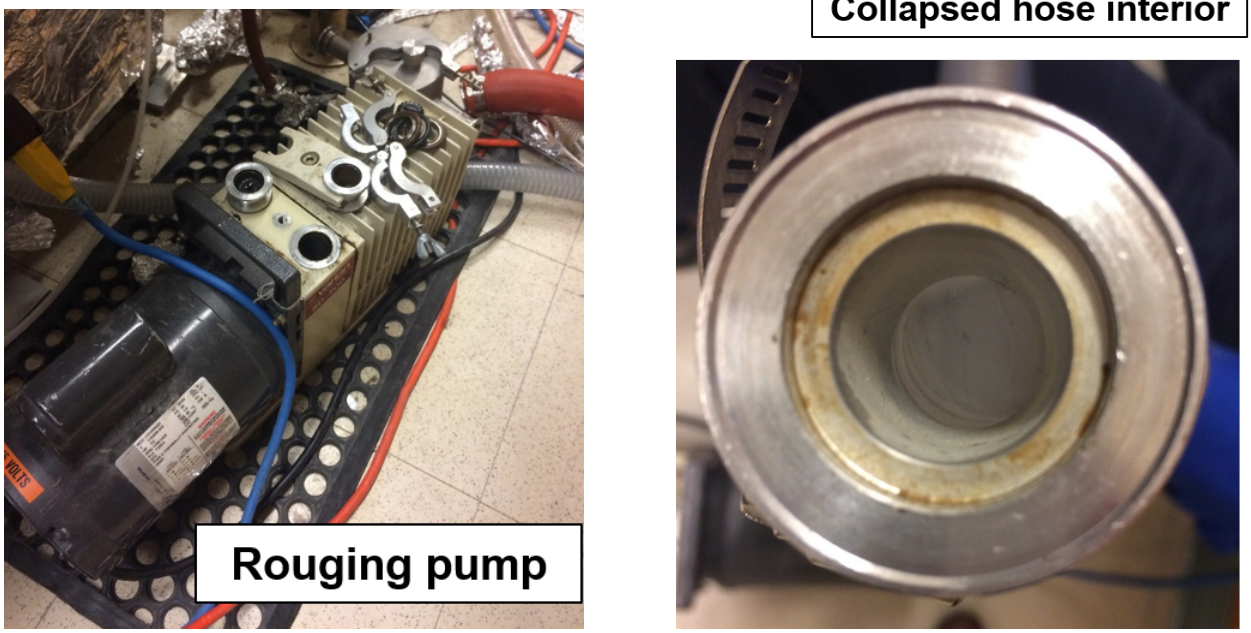

Figure 2.11 (Left) The roughing pump connecting to the dipstick and acting as the first line of defense. (Right) The interior wall of the connecting hose collapsed and prevented proper operation of the roughing pump. Replacement of this hose resolved the apparent leak.

CHAPTER 3: POROUS GRAPHENE NANORIBBONS ON SEMICONDUCTOR SUBSTRATES

3.1 Porous Graphene Nanoribbon Background

The bottom-up wet chemical synthesis of graphene nanoribbons (GNRs) opens interesting opportunities for tailoring the GNR structure with atomic precision [29]. Bottom-up fabrication of GNRs relies on the formation of precursor molecules into polymer chains followed by cyclodehydrogenation. Changing the precursor molecule affects how the molecules bond together to form the polymer chains and the final GNR structure. Atomically precise porous GNRs are a new chemically synthesized variation for which the fabrication procedure yielding multiple pores in a single ribbon and the electronic details of the ribbon have not been reported. Porous GNRs have potential applications in molecular filtration, detection and DNA sequencing.

In this work, porous GNRs are dry contact transferred in ultrahigh vacuum to clean silicon and III-V semiconducting substrates and examined using UHV scanning tunneling microscopy (STM) and spectroscopy (STS). The porous GNRs in this work are synthesized by the Sinitskii Group at the University of Nebraska. The structure of the porous GNR is similar to the chevron GNR except that an additional bond between carbon atoms closes what would be the periodic bends in the chevron GNR. The edge termination is of the armchair geometry. The top image in Figure 3.1 is the schematic of this porous GNR.

STM imaging confirms the expected porous structure and indicates a unique electronic feature at the graphene nanopores, and STS measurements indicate a 2.0 eV bandgap. Illumination of pore effects in GNRs contributes to an increased understanding of the tunability of GNR electronic structure.

3.2 Porous Graphene Nanoribbon Initial Experiments

Initial STM experiments confirm the expected porous structure and indicate a 1.7 nm periodicity of the pore [39]. The relative height of the GNR is 2.1 Å. The pores appear as protrusions with a height of 3.6 Å relative to the substrate, indicating a unique electronic feature at the pores. Furthermore, semitransparency of the ribbon enables visibility of the silicon dimer rows beneath the GNRs.

Scanning tunneling spectroscopy measurements indicate a 1.76 eV bandgap at the edge and a 2.73 eV bandgap at the center of the GNR. Figure 3.1 (a) is an STM image of the porous GNR on H:Si(100). The dimer rows of the silicon dangling bonds are visible as well as the GNR pores. Figure 3.1 (b) is the corresponding height profile for the GNR along lines 1 and 2 in image (a). The height profile indicates the GNR height of 2.1 Å relative to the substrate and the electronic height of the pores of 3.6 Å relative to the substrate [39].

In order to fully understand the effects of the pores on the bandgap, more spectroscopy data is necessary. The initial experiments on H:Si(100) demonstrated a highly diffusive nature of the GNRs on the substrate. In order to mitigate the problem of these GNRs diffusing on the passivated silicon surface, experiments on III-V semiconductors are of interest due to the material's more reactive surface. Illumination of pore effects in GNRs contributes to an increased understanding of the tunability of GNR electronic structure.

3.3 Investigations of Porous Graphene Nanoribbons on InAs

Preparation of an InAs substrate varies from that of silicon due to the use of the substrate cross-section rather than the surface as in the case of silicon. The first step in preparation is modifying the sample holder in order to clamp the substrate such that the edge extends outward.

A diamond scribe is used *ex situ* to scribe a line along the edge of the sample holder clamp to promote clean cleaving. The sample holder is then mounted to the dipstick in the preparation chamber and degassing takes place using the tantalum filament. The top left image in Figure 3.2 shows the InAs substrate in the sample holder before cleaving.

After degassing, titanium is evaporated onto the sample holder to help prevent impurities from contaminating the cleaved InAs surface. Cleaving takes place in the STM chamber while the sample holder is on the linear transverse motion (LTM) fork. The wobble stick in the STM chamber, used for moving pieces around on the STM stage, is used to carefully cleave the InAs on the side of the scribe mark. The top right image in Figure 3.2 shows the mirror-like InAs cross-section surface revealed after the cleaving procedure. An optical microscope is then used to view the STM from the outside of the UHV chamber in order to align the STM tip with the cross-section. This is a non-trivial step that can result in damage to the STM tip if not aligned properly. The bottom image in Figure 3.2 is the top-down view in the optical microscope of the STM tip aligned with the InAs cross-section.

Initial STM scans of the cleaved InAs substrates prior to DCT of GNRs revealed the substrates were not cleaving along a single plane. Instead, numerous terraces were observed along with the atomic rows. Figure 3.3 shows the poor quality of the cleaved surfaces observed using the STM. Here we see the numerous terraces as well as the atomic rows at a scanning bias of V_{bias}= -0.5 V. Terraces are non-ideal for GNR experiments due to the messiness of the substrate and how that can affect GNR interactions with the substrate and subsequent measurements. Furthermore, GNRs are extremely difficult to locate on a messy substrate and extensive experimental time is wasted.

After numerous iterations of sample preparation and cleaving, it was discovered that the quality of the cleave depends on the degassing temperature. Degassing at temperatures around 150°C resulted in very clean cleaves. Figure 3.4 is an STM image of a clean cleaved InAs surface. The white dashed lines are a result of slight tip instability. The atomic rows are easily observed. Another challenge arose, however, in that stable scans were not achieved at a positive bias. The top image in Figure 3.4 is at V_{bias}= -1.5 V. The bias was then switched to V_{bias}= +1.5 V and did not result in a stable scan. The bottom image in Figure 3.4 is the following image in this three-scan sequence. Here we see numerous atoms deposited in the same area as the top image as a result of scanning at a positive bias. Consistent scans at both positive and negative biases are required for reliable spectroscopy data that ramps voltages between negative and positive bias.

After achieving a clean cleaved InAs surface, the porous GNRs were applied to the surface via DCT. Initial scans reveal features of the expected GNR height. Figure 3.5 shows an STM image at V_{bias}= -1.5 V of a possible GNR with corresponding height profile. The height profile indicates the height of the feature to be 2.6 Å relative to the surface. This value is similar to that in the initial experiments on silicon.

3.4 Summary and Future Work

Initial STM scans of the porous GNR on H:Si(100) confirm the expected structure and reveal a GNR height of 2.1 Å relative to the substrate and a pore height of 3.6 Å relative to the substrate. STM experiments reveal a pore periodicity of 1.7 nm. A bandgap of 1.76 eV at the GNR edge and a bandgap of 2.73 eV at the GNR center are measured using scanning tunneling spectroscopy [39]. A highly diffusive nature of the porous GNR on the substrate is observed in the

STM experiments. The cross-section of InAs is explored as a viable substrate in order to mitigate the diffusive nature of the GNR on passivated silicon.

Future work includes further STM experiments on the porous GNR on III-V semiconductor substrates. Investigations using passivated silicon and desorbing hydrogen would reveal highly reactive regions that would be ideal for GNR experiments. Further data on the bandgap is required in order to fully understand the effect of pores in GNRs.

3.5 Figures

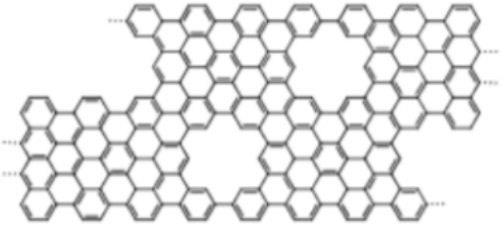

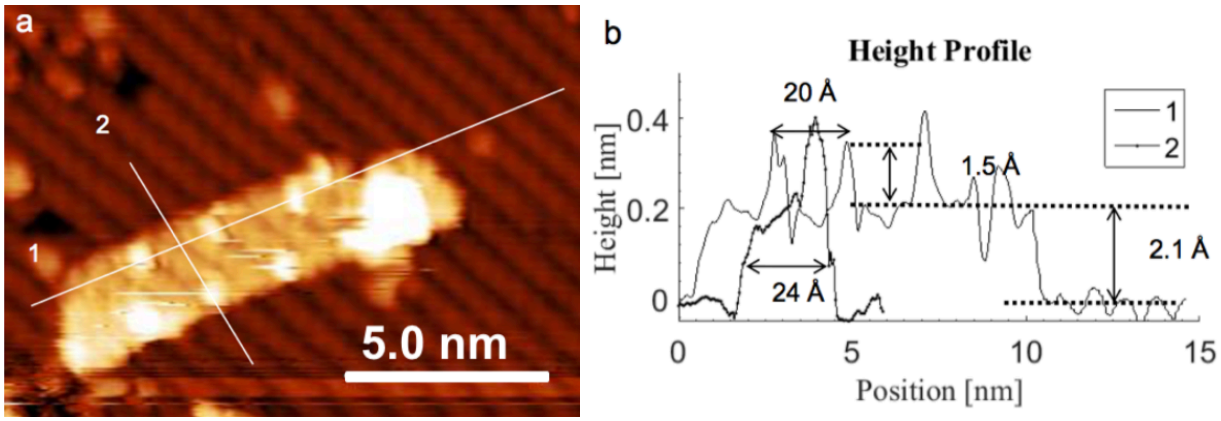

Figure 3.1 (Top) Porous GNR schematic. (a) STM image on H:Si(100) (Room-temperature, V=-3 V, I=10 pA). (b) Height profile corresponding to porous GNR in (a). GNR height is 2.1 Å relative to substrate. Pore height is 3.6 Å relative to substrate [39].

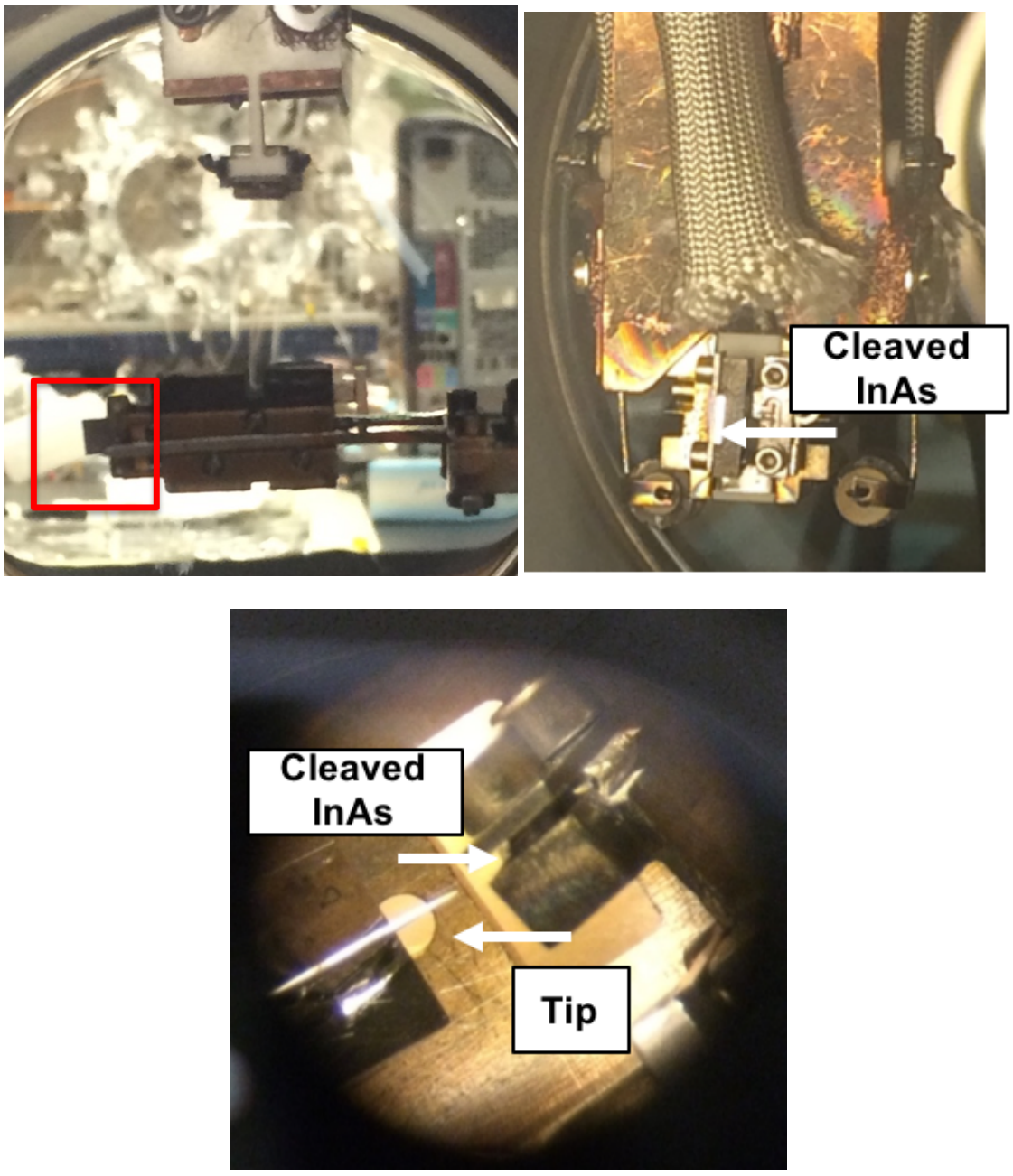

Figure 3.2 InAs sample preparation *in situ* for GNR experiments. (Top left) InAs is scribed *ex situ* and mounted to sample holder such that the cross-section faces out into the chamber. (Top right) Sample holder is mounted in the dipstick. Cross-section of InAs after cleaving *in situ* is observed as a mirror like surface. (Bottom) An optical microscope is used to view the STM tip and top of the sample holder in order to align the STM tip with the InAs cross-section.

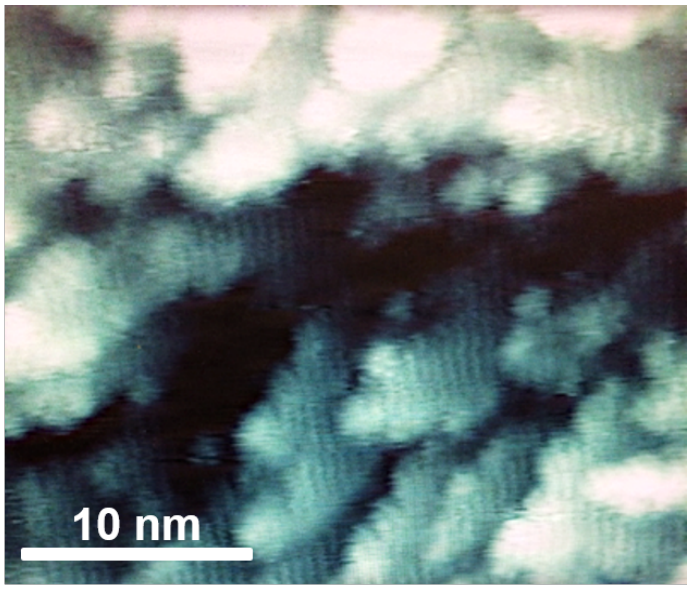

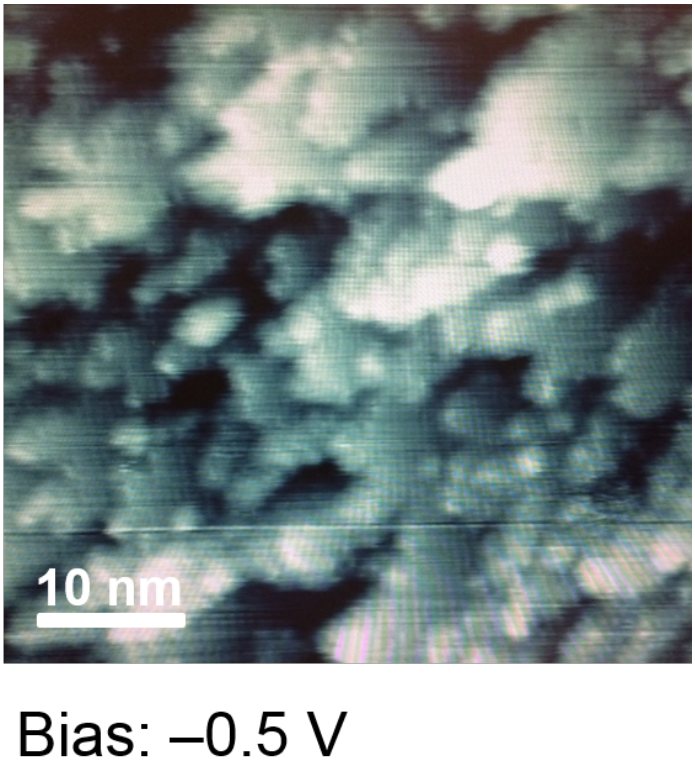

Figure 3.3 Initial STM scans of an InAs(110) cross-section reveal numerous terraces. Both images are STM scans at V_{bias}= -0.5 V. The atomic rows of the InAs substrate are observed.

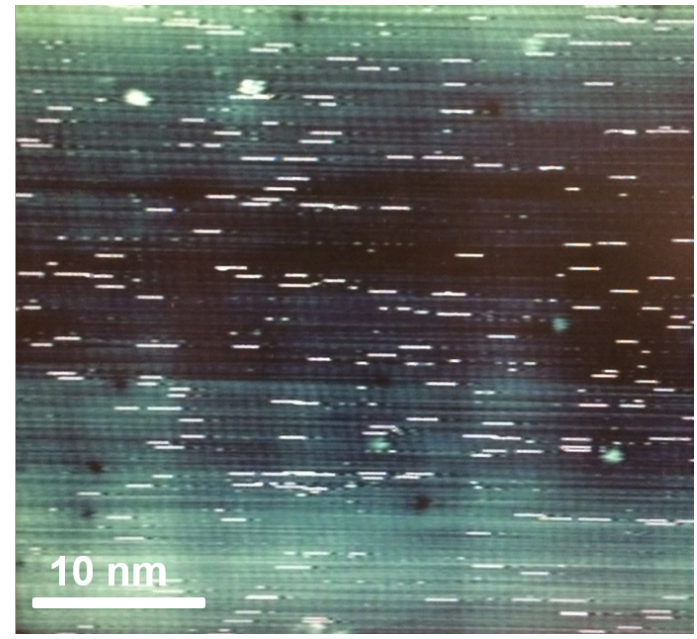

Figure 3.4 STM images at V_{bias} = -1.5 V of clean cleaved InAs(110) cross-section substrate. White dashed lines are slight tip instabilities. Atomic rows are observed in both images. After scanning the top image, a scan at positive V_{bias} = +1.5 V followed, which failed to result in a stable scan. The bottom image here is the subsequent scan revealing atomic deposition from the tip during the positive bias scan.

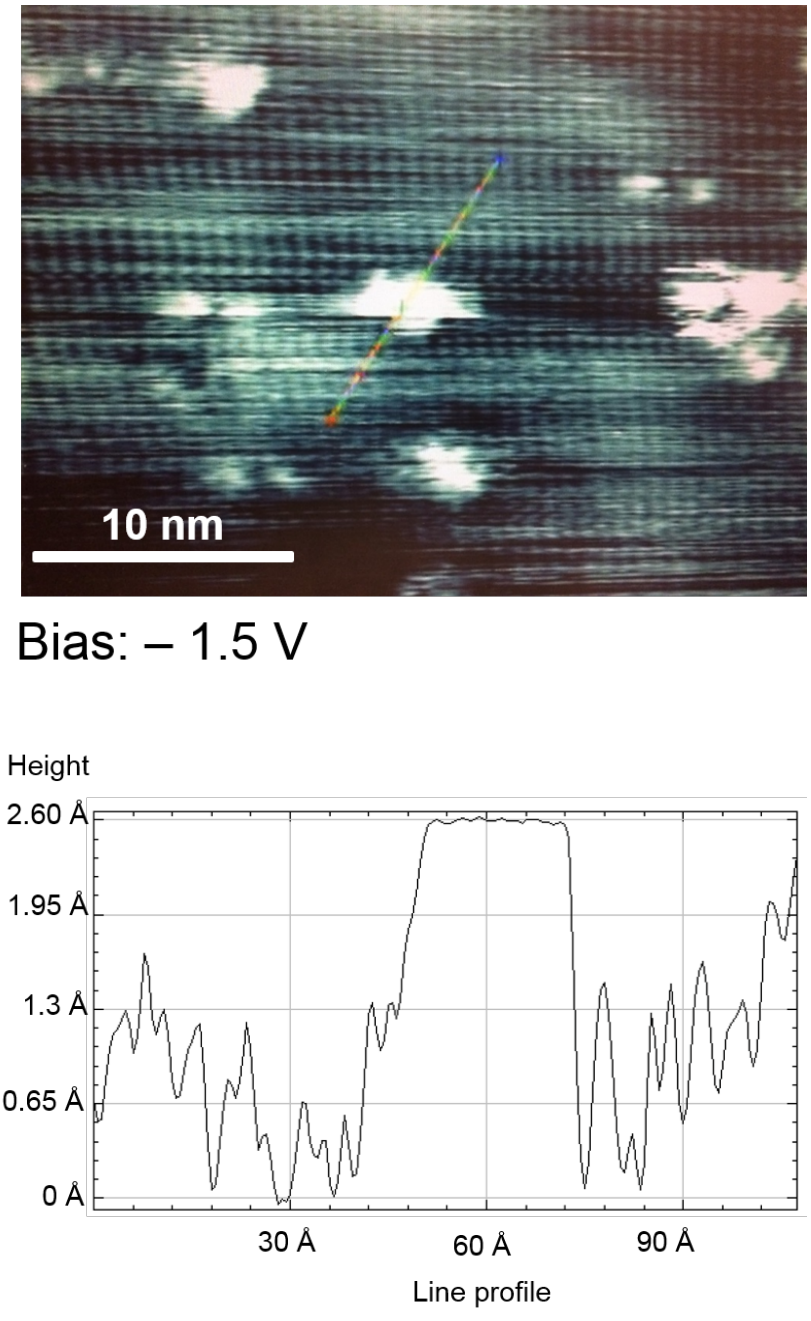

Figure 3.5 STM scan at V_{bias} = -1.5 V on InAs cross-section substrate. Features observed in STM image after DCT of porous GNR. The height profile corresponds to the line in the top image indicating a height of 2.1 Å for the potential GNR feature.

CHAPTER 4: SUMMARY AND OUTLOOK

In summary, UHV chamber modifications and maintenance were accomplished, and graphene nanoribbon experiments were conducted. The entire UHV system was first vented. The STM chamber received repairs to the STM stage and electrical connections. An extended titanium sublimation pump was added in the STM chamber to reduce impurities on the stage and prevent impurities from diffusing onto the clean substrates. The preparation chamber received the addition of a cracking filament necessary for silicon passivation with hydrogen. The dipstick in the preparation chamber received an innovation for degassing substrates indirectly and a design overhaul. Challenges arose, including an electrical short in the preparation ion pump preventing normal operation, the failure of two turbo pumps and a collapsed interior wall of the hose connecting the dipstick to the roughing pump. The final bake-out base pressure was 9×10^{-11} Torr.

Atomically precise porous GNRs were dry contact transferred to silicon and III-V semiconductor substrates and investigated using UHV STM and STS. STM confirms the porous structure and indicates the pores as electronic protrusions. The GNR height is 2.1 Å and the pore height is 3.6 Å relative to the substrate.

Future work includes further investigations of the porous GNR on InAs cross-section substrates and the collection of more spectroscopy data in order to fully understand the effect of the pore on the electronic properties of the GNR. Future UHV work includes moving the four STM systems to the new lab space in the Micro and Nanotechnology Laboratory and the Electrical and Computer Engineering Building.

REFERENCES

[1] J. Loughran, "Intel's 10 nm Technology: Delivering the Highest Logic Transistor Density in the Industry Through the Use of Hyper Scaling." Retrieved March 26, 2018, from https://newsroom.intel.com/newsroom/wp- content/uploads/sites/11/2017/09/10-nm-icf-fact-sheet.pdf (2017).

[2] M. Bohr, "Integrated circuit scaling to 10 nm and beyond." Retrieved March 26, 2018, from https://www.youtube.com/watch?v=ApWOf6J858Y (2018, January 30).

[3] K. S. Novoselov, A. K. Geim, S. V. Morozov, D. Jiang, Y. Zhang, S. V. Dubonos, I. V. Grigorieva and A. A. Firsov, "Electric field effect in atomically thin carbon films," *Science* **306** 666 (2004).

[4] R. E. Peierls, "Quelques proprieties typiques des corpses solides," *Ann. I. H. Poincare* **5** 177 (1935).

[5] L. D. Landau, "Zur theorie der phasenumwandlungen II," *Phys. Z. Sowjetunion* **11** 26 (1937).

[6] J. A. Venables, G. D. T. Spiller and M. Hanbucken, "Nucleation and growth of thin films," *Rep. Prog. Phys.* **47** 399 (1984).

[7] J. W. Evans, P. A. Thiel and M. C. Bartelt, "Morphological evolution during epitaxiam thin film growth: Formation of 2D islands and 3D mounds," *Sur. Sci. Rep.* **61** 1 (2006).

[8] K. S. Novoselov, D. Jiang, F. Schedin, T. J. Booth, V. V. Khotkevich, S. V. Morozov and A. K. Geim, "Two-dimensional atomic crystals," *PNAS* **102** (30) 10451 (2005).

[9] K.I. Bolotin, K.J. Sikes, Z. Jiang, M. Klima, G. Fudenberg, J. Hone, P. Kim, and H.L. Stormer, "Ultrahigh electron mobility in suspended graphene," *Solid State Comm.* **146** 351 (2008).

[10] A. S. Mayorov et al. "Micrometer-scale ballistic transport in encapsulated graphene at room temperature," *Nano. Lett.* **11** 2396 (2011).

[11] S. V. Morozov et al. "Giant intrinsic carrier mobilities in graphene and its bilayer," *Phys. Rev. Lett.* **100** 016602 (2008).

[12] C. Lee, X. D. Wei, J. W. Kysar and J. Hone, "Measurement of the elastic properties and intrinsic strength of monolayer graphene," *Science* **321** 385 (2008).

[13] F. Liu, P. M. Ming and J. Li, "Ab initio calculation of ideal strength and phonon instability of graphene under tension," *Phys. Rev. B* **76** 064120 (2007).

[14] K. S. Novoselov et al. “Two-dimensional gas of massless Dirac fermions in graphene,” *Nature* **438** 197 (2005).

[15] Y. Zhang, J. W. Tan, H. L. Stormer and P. Kim, “Experimental observation of the quantum Hall effect and Berry’s phase in graphene,” *Nature* **438** 201 (2005).

[16] A. K. Geim and K. S. Novoselov, “The rise of graphene,” *Nature Materials* **6** 183 (2007).

[17] J. Cai, P. Ruffieux, R. Jaafar, M. Bieri, T. Braun, S. Blankenburg, M. Muoth, A. P. Seitsonen, M. Saleh, X. Feng, K. Müllen and R. Fasel, “Atomically precise bottom-up fabrication of graphene nanoribbons,” *Nature* **466** 470 (2010).

[18] L. Chen, L. Wang, and D. Beljonne, “Designing coved graphene nanoribbons with charge carrier mobility approaching that of graphene,” *Carbon* **77** 868 (2014).

[19] N. D. Arora, J. R. Hauser, and D. J. Roulston, “Electron and hole mobilities in silicon as a function of concentration and temperature,” *IEEE Trans. on Electron Devices* **ED-29** 2 (1982).

[20] M. Y. Han, B. Özyilmaz, Y. Zhang and P. Kim, “Energy band-gap engineering of graphene nanoribbons,” *Phys. Rev. Lett*. **98** 206805 (2007).

[21] X. Jia, J. Campos-Delgado, M. Terrones, V. Meuniere and M. S. Dresselhaus, “Graphene edges: a review of their fabrication and characterization,” *Nanoscale* **3** 86 (2011).

[22] N. Merion-Díez, J. Li, A. Garcia-Lekue, G. Vasserur, M. Vilas-Varela, E. Carbonell-Sanromà, M. Corso, J. E. Ortego, D. Peña, J. I. Pascual, and D. G. de Oteyza, “Unraveling the electronic structure of narrow atomically precise chiaral graphene nanoribbons,” *J. Phys. Chem. Lett.* **9** 25 (2018).

[23] L. Tapasztó, G. Dobrik, P. Lambin and L. P. Biró, “Tailoring the atomic structure of graphene nanoribbons by scanning tunneling microscope lithography,” *Nature Nano.* **3** 397 (2008).

[24] L. Brey, and H. A. Fertig, “Electronic states of graphene nanoribbons studied with the dirac equation,” *Physical Rev. B* **73** 23 (2006).

[25] K. Nakada, M. Fujita, G. Dresselhaus, and M. S. Dresselhaus, “Edge state in graphene ribbons: Nanometer size effect and edge dependence,” *Phys. Rev. B* **54** (24) 17954 (1996).

[26] C. Tao et al. “Spatially resolving edge states of chiral graphene nanoribbons,” *Nature Phys.* **7** 616 (2011).

[27] A. Luican, G. Li, and E. Y. Andrei, “Scanning tunneling microscopy and spectroscopy of graphene layers on graphite,” *Solid State Comm.* **149** 1151 (2009).

[28] X. Wang and H. Dai, "Etching and narrowing of graphene from the edges," *Nature Chem.* **2** 661 (2010).

[29] T. Vo, M. Shekhirev, D. A. Kunkel, M. D. Morton, E. Berglund, L. Kong, P. M. Wilson, P. A. Dowben, A. Enders and A. Sinitskii, "Large-scale solution synthesis of narrow graphene nanoribbons," *Nature Comm.* **5** 3189 (2014).

[30] R. Miranda, N. García, A. M. Baró, R. García, J. L. Peña and H. Rohrer, "Technological applications of scanning tunneling micrscopy at atmospheric pressures," *Appl. Phys. Lett.* **47** 367 (1985).

[31] J. W. Lyding, T.-C. Shen, J. S. Hubacek, J. R. Tucker and G. C. Abeln, "Nanoscale patterning and oxidation of H-passivated Si(100)-2x1 surfaces with an ultrahigh vacuum scanning tunneling microscope," *Appl. Phys. Lett.* **64** (15) 2010 (1994).

[32] R. J. Hamers, R. M. Tromp and J. E. Demuth, "Scanning tunneling microscopy of Si(001)," *Phys. Rev. B* **34** (8) 5343 (1986).

[33] J. Repp, G. Meyer, S. M. Stojkocić, A. Gourdon and C. Joachim, " Molecules on insulating films: scanning-tunneling microscopy imaging of individual molecular orbitals," *Phys. Rev. Lett.* **94** 026803 (2005).

[34] C. Julian Chen. *Introduction to Scanning Tunneling Microscopy.* Oxford University Press New York, 1993.

[35] G. Binning and H. Rohrer, "Scanning tunneling microscopy," *IBM J. Res. Dev.* **30** (4) (1986).

[36] P. M. Albrecht and J. W. Lyding, "Ultrahigh-vacuum scanning tunneling microscopy and spectroscopy of single-walled carbon nanotubes on hydrogen-passivated Si(100) surfaces," *Appl. Phys. Lett.* **83** 5029 (2003).

[37] K. A. Ritter and J. W. Lyding, "The influence of edge structure on the electronic properties of graphene quantum dots and nanoribbons," *Nature Materials* **8** 235 (2009).

[38] A. Radocea, T. Sun, T. Vo, A. Sinitskii, N. R. Aluru and J. W. Lyding, "Solution-synthesized chevron graphene nanoribbons exfoliated onto H:Si(100)," *Nano Lett.* **17** 170 (2016).

[39] A. Radocea, "Scanning tunneling microscopy investigation of atomically precise graphene nanoribbons," dissertation, University of Illinois Urbana-Champaign (2017).

[40] B. Murphy, thesis, Trinity College Dublin (2014).